Frontal-wave cyclogenesis in the North Atlantic – a climatological characterisation

Sebastian Schemm[a]* and Michael Sprenger[b]

[a]*Geophysical Institute, University of Bergen and Bjerknes Centre for Climate Research, Norway*
[b]*Institute for Atmospheric and Climate Science, ETH Zürich, Switzerland*

Correspondence to: S. Schemm, Geophysical Institute, University of Bergen, Allégaten 70, NO-5007 Bergen, Norway.
E-mail: sebastian.schemm@gfi.uib.no

The ambient conditions during cyclogenesis on fronts in the North Atlantic (NA) are characterised climatologically in the ERA-Interim dataset. These 'secondary' cyclones, which grow from frontal waves, are typically small in scale, shallow and deepen rapidly, and pose a challenge to forecasters and numerical weather prediction models. Frontal-wave development has been studied intensively in the past based on observations (e.g. FASTEX), real-case studies or analytical models. In this study, frontal-wave cyclogenesis is studied from a climatological perspective and is detected by a combination of two automated identification methods for the period between 1979 and 2014. A climatology of frontal-wave cyclogenesis is presented. Horizontal composites provide an estimate of the climatological mean of conditions during frontal-wave cyclogenesis which may prove useful in the assessment of the realism of proposed idealized models of frontogenesis. The findings are also compared with assumptions made in earlier idealized studies of frontal waves. The composites reveal coherent structures of diabatically generated low-level PV in the lower troposphere, neutral moist static stability at cyclogenesis and an ambient lower troposphere close to saturation. The vertical PV structure in the east NA is more vertically aligned than in the west NA and PV anomalies from the upper and lower levels reach deeper into the mid-troposphere, which indicates an enhanced phase-lock between the two anomalies. Previous studies suggest the existence of an upper limit of along-frontal stretching above which frontal-wave development is strongly suppressed. The presented multi-decadal analysis confirms its existence in a range between 0.6 and 0.8×10^{-5} s^{-1}. Finally a climatology of along-frontal stretching for the NA is presented and compared to the fraction of cyclogenesis forming on frontal waves.

Key Words: frontal wave; cyclogenesis; climatology; along-frontal stretching; potential vorticity; deformation; secondary cyclogenesis

Received 26 November 2014; Revised 12 May 2015; Accepted 14 May 2015; Published online in Wiley Online Library 14 July 2015

1. Introduction

The birth of a cyclone in the midlatitudes may be attended by a strong surface front, an upper-level trough or a combination of both. Conceptual descriptions of cyclogenesis on fronts date back at least to the ground-breaking work of the Bergen School of Meteorology in the 1920s (Bjerknes and Solberg, 1922) and their concept of a 'polar front'. There is considerable observational evidence for cyclogenesis on fronts (Appenzeller and Davies, 1996; Rivals *et al.*, 1998; Chaboureau and Thorpe, 1999), which is often referred to as secondary cyclogenesis because the underlying front initially trails a major depression (the 'primary' cyclone), henceforth frontal-wave cyclogenesis for short; see the review article by Parker (1998) and the FASTEX overview by Baehr *et al.* (1999).

Schär and Davies (1990) and Joly and Thorpe (1990) derived an underlying theoretical framework for the (until then) observation-based concept of frontal instability, i.e. the intrinsic instability of a mature front, in a semi-geostrophic analytical model. They showed that a banded along-frontal positive potential temperature (θ) (Schär and Davies, 1990) or potential vorticity (PV) anomaly (Joly and Thorpe, 1990), placed ahead of a cold front, prescribes a frontal instability configuration which results in the growth of a frontal wave. The resulting instability type shares characteristics of a mixed baroclinic–barotropic (Schär and Davies, 1990) or pure barotropic (Joly and Thorpe, 1990) instability for the most unstable mode. The differences in the energetics between the identified frontal waves in their models stem from the width of the chosen PV or θ anomaly band ahead of the cold front. The instability of an along-frontal PV band was also proposed by

Thorpe and Emanuel (1985) in their study on slantwise convection in a frontal zone. However, a number of physical mechanisms which can significantly modulate frontal-wave cyclogenesis are described in the literature, such as latent heat release (Hoskins and Berrisford, 1988; Reed *et al.*, 1993) and large-scale strain (Dritschel *et al.*, 1991; Bishop and Thorpe, 1994b; Dacre and Gray, 2006). The formation of an along-frontal PV band by latent heat release is simulated for example by Thorpe and Emanuel (1985) in a strain field and by Emanuel *et al.* (1987) in a pure shearing zone.

From a more conceptual viewpoint, frontal-wave development can be regarded, following the theoretical consideration of Bishop and Thorpe (1994b) and a later summary by Dacre and Gray (2006), as a two-step process:

- A strengthening of the front by increasing deformation, which causes upward motion on the warm side of the front. Latent heat release leads to the formation of a PV strip along the front.
- A reduction in deformation causes the PV strip to break into individual PV anomalies. Frontal waves develop from the associated cyclonic vorticity field and can transform into a distinct low if the growth rate of the frontal wave overcomes the growth rate of the front.

The reduction of deformation, or the cessation of frontogenesis, is a crucial aspect for the continuous growth of the frontal wave into a distinct low pressure system. As shown by Renfrew *et al.* (1997), strong stretching can suppress the growth of along-frontal instabilities by flattening frontal waves. Likewise, if the stretching is rather weak compared to the frontal (potential) vorticity strip, instabilities may amplify. Similar findings were made in the observational studies of Rivals *et al.* (1998) and Chaboureau and Thorpe (1999). During the translation, the driving instability transforms from a barotropic into a classical baroclinic type of growth mechanism (Malardel *et al.*, 1993), which includes the phase-locking with an upper-tropospheric flow anomaly (e.g. a trough or a PV streamer).

A series of observational frontal-wave studies (Renfrew *et al.*, 1997; Rivals *et al.*, 1998; Chaboureau and Thorpe, 1999) supported the theoretical analysis of frontal-wave growth by Bishop and Thorpe (1994b), whose analytical model predicted that frontal-wave growth is very unlikely in persistent strain rates greater than $0.6 \times 10^{-5}\,\mathrm{s}^{-1}$. However the observational findings are based upon only a limited sample size and therefore cannot confidently reject the null hypothesis that along-frontal strain has no suppressive effect. This motivates a multi-decadal analysis of along-frontal stretching over the ERA-Interim period to have a sufficiently large sample size. Additionally, the (Bishop and Thorpe, 1994b) analytical model predicts that all frontal wave growth due to barotropic edge-wave interaction is suppressed for along-front stretching rates greater than $0.25 f \sim 2.5 \times 10^{-5}\,\mathrm{s}^{-1}$, where f denotes the Coriolis parameter. Previous case-studies identified strain rates of up to $1.6 \times 10^{-5}\,\mathrm{s}^{-1}$ (Renfrew *et al.*, 1997).

Baroclinic amplification of the frontal wave is described by Hoskins *et al.* (1985) as the phase-lock between an upper- and lower-level wave anomaly, e.g. in terms of PV anomalies. The importance of the two PV anomalies in the lower and upper troposphere and their mutual interaction for successful frontal-wave growth is revealed in a study by Fehlmann and Davies (1999). In their set of simulations, they consider a real-case frontal-wave development and explore its life cycle under perturbed initial conditions, i.e. by the removal of the upper- or lower-level PV anomaly in the initial conditions. The omission of the upper-tropospheric PV anomaly results in a cessation of the development, while the removal of the surface initial PV anomaly is countered by the prompt diabatic growth of new PV anomalies and the subsequent growth of sub-synoptic cyclones. According to the findings of Fehlmann and Davies (1999), the fine-scale structure of the low-level PV anomaly is not a central aspect, however

the interaction with the upper-level PV anomaly is intrinsic to the cyclogenesis. Likewise Renfrew *et al.* (1997) show in their comparison of developing and non-developing frontal waves over the North Atlantic (NA) that the phase-lock with an upper-level flow anomaly is a key ingredient for the further deepening during the second stage of the development. Similar findings are suggested in a frontal-wave case-study by Appenzeller and Davies (1996), who also describe several distinct frontal-wave developments from a PV perspective, e.g. tip vortices developing at the end of a PV band versus low-level instabilities of enhanced PV bands. Finally the importance of the upper-level PV anomaly is also highlighted by Zhang *et al.* (2002) in their study of three frontal-wave events over the western NA, using a similar PV inversion strategy as Fehlmann and Davies (1999). The authors also underpin the importance of the relative position to the jet, with the anticyclonic-shear side of the jet being less favourable for frontal-wave development if the growth is not strongly dominated by diabatic mechanisms, e.g. latent-heat release in the lower troposphere or surface fluxes. One of the first preliminary climatologies with a focus on sub-synoptic time and spatial scales, i.e. different band-pass filtered high frequencies in the vorticity field, is the work by Ayrault *et al.* (1995). However they focused on the entire spectrum of high frequencies and not specifically on frontal waves.

Besides the two pertinent fields, PV and deformation, we draw our attention in this study also toward other key fields such as precipitation, heat and moisture fluxes and stability, to compile a catalogue of characteristic ambient conditions during frontal-wave cyclogenesis. More precisely we aim to

(i) identify preferred regions of cyclogenesis on frontal waves in the NA based on the combination of two automated identification methods;

(ii) characterise the ambient state of the atmosphere by making composites of horizontal and vertical cross-sections of selected fields. The latter focuses on the vertical PV structure and the upper-level flow anomaly. The former on ambient deformation, precipitation, stability and surface fluxes among others. The thereby derived composites may help guide the design of future idealized model experiments. Based on the composites, we also comment on assumptions made in idealised set-ups of earlier studies, e.g. Bishop and Thorpe (1994a; 1994b); and

(iii) derive an empirical threshold for the along-frontal stretching rate of the ambient wind above which frontal-wave development is largely suppressed and compare it to the results derived from theoretical models. We also address two hypotheses of Bishop and Thorpe (1994b), who suggest all frontal-wave growth (due to barotropic edge waves) is suppressed for along-frontal stretching greater than $2.5 \times 10^{-5}\,\mathrm{s}^{-1}$ and is still very unlikely at strain rates greater than $0.6 \times 10^{-5}\,\mathrm{s}^{-1}$.

1.1. Outline

After a detailed introduction into the front and cyclone identification schemes (section 2.1), two examples which illustrate the procedure are discussed in section 2.2. Thereafter a climatology of trailing fronts and frontal waves is presented in section 3. The dynamical relevance of the thereby detected frontal waves is highlighted in section 4, where horizontal composites reveal significant values of diabatically generated lower tropospheric PV, strong deformation and high precipitation rates. Consideration is also given to the vertical structure of frontal wave cyclogenesis (section 5), before we turn to the analysis of along-frontal stretching rates (section 6).

2.   Data, methodology and analysis framework

The methodological base upon which this study is built is outlined below. To automatically identify frontal-wave cyclogenesis in a

larger framework over multi-decades, a combination of two automated identification strategies is required. In this study the parent techniques are the cyclone detection and tracking method of Wernli and Schwierz (2006) applied in conjunction with the frontal identification strategy of Hewson (1998), as implemented by Jenkner *et al.* (2010) and proceeded by Schemm *et al.* (2014). The dataset is ERA-Interim (Dee *et al.*, 2011) interpolated on a $1° \times 1°$ grid. The considered time period spans the years from 1979 to DJF 2013/14 in 6 h time steps.

In the following, a more detailed introduction to the applied methods and the analyses procedures is given.

2.1. Identification strategies for fronts, cyclogenesis and frontal-wave cyclogenesis

2.1.1. Front identification

The front identification as in Schemm *et al.* (2014) is used. Fronts are required to have a minimum gradient of equivalent potential temperature of $4 \, \text{K} \, (100 \, \text{km})^{-1}$ at 850 hPa and a minimum length of 500 km. This ensures the detection of synoptic-scale fronts which have already grown a significant length prior to cyclogenesis. Thereby they also become distinct and separated from local zones of weak baroclinicity. If two fronts are detected within a radius of 300 km, they are combined into one front. This threshold tolerance accounts for gaps in the strength of the gradient, which can be expected during the cessation of frontogenesis at cyclogenesis. In addition, quasi-stationary fronts are removed by a minimum advection threshold $(3 \, \text{m} \, \text{s}^{-1})$. Otherwise various types of thermal boundaries are frequently detected by frontal identification methods based on thermal gradients. These quasi-stationary fronts are typically identified along coastlines (i.e. land–sea breezes) or along steep topography (the discussion in Schemm *et al.*, 2014, gives more details on this issue). For the purpose of this study, these kind of fronts are not relevant and are therefore excluded.

The settings and parameters have been tested in great detail in the intercomparison study of Schemm *et al.* (2014), in which two commonly used frontal identification strategies are contrasted in various synoptic situations. The authors showed that the thermal method as applied in this research has strong skills in the recognition of cold and warm fronts in the NA. In contrast, a wind-based method, e.g. Simmonds *et al.* (2012), has stronger skill detecting shallower shear-induced fronts, in particular in the Southern Hemisphere.

2.1.2. Cyclone identification and tracking

The applied cyclone identification strategy of Wernli and Schwierz (2006) is based on the detection of closed sea-level pressure (SLP) contours. The scheme also includes a tracking of cyclones. All cyclones taken into account are required to persist for at least 24 h. Note that, by design of the identification strategy, cyclogenesis is recognised as the occurrence of the first closed isobar and hence differs from the onset of frontal instability, i.e. the onset of wave-like anomalies on the front prior to the break-up of the PV band. More precisely, cyclogenesis is identified at the location of minimum SLP inside the closed isobar. Typically the first closed isobar is identified after the break-up of the along-frontal PV band and hence after the translation from a barotropic frontal wave into a baroclinic depression with self-contained vertical motion and circulation.

2.1.3. The detection of frontal-wave cyclogenesis

All cyclogenesis cases which are located on a *trailing front* are considered to be frontal-wave cyclogenesis events. By definition, a trailing front is a front which is attending a parent cyclone, i.e. the front is overlapping with one of the cyclone's closed sea-level isobars. A tolerance in the distance between a trailing front and the precise cyclogenesis location of 100 km is accepted. This constraint requires the cyclogenesis location to be on a grid-point which equally is identified as a frontal grid-point or on one of its eight neighbouring grid-points. Any cyclone can serve as parent cyclone at any time during its life cycle except during its own cyclogenesis. This procedure to identify frontal-wave cyclogenesis on trailing fronts bounds the analysed cases in this study closely to the archetypical frontal-wave cyclogenesis examples examined during the Fronts and Atlantic Storm-Track Experiment (FASTEX) field campaign.
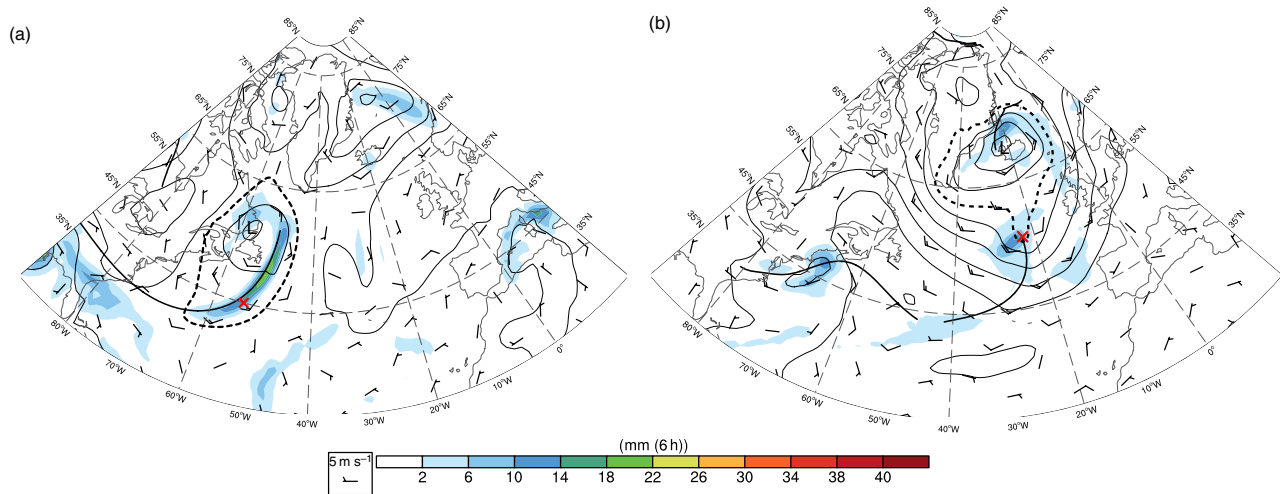
As eastern NA frontal waves are known to deepen rapidly (Parker, 1998), and since earlier studies on cyclonic life cycles suggest different characteristics in the eastern and western NA, e.g. the minimum SLP of a cyclone is on average lower in the eastern NA (Dacre and Gray, 2009), the two basins are analysed separately from here.

2.2. Automated detection of frontal-wave cyclogenesis: two illustrative examples

To give an impression of identified frontal-wave cyclogenesis events, two examples are shown in Figure 1. The first example is located in the western NA over the Gulf Stream region (Figure 1(a)) and the second example is located in the eastern NA (Figure 1(b)). In both examples the outermost contour of the parent low, indicated by **L**, is dashed and the frontal-wave cyclogenesis is marked with a red cross.

In the first example located at 0600 UTC on 29 October 1985 in the western NA, the parent cyclone is situated at 56°W, 52°N, in the Strait of Belle Isle slightly north of Newfoundland. A long and elongated cold front extends from the low southwards to 36°N, where it turns zonally towards the American continent. The outermost closed sea-level isobar (dashed) of the cyclone is intersecting the front and hence this front is assumed to be a trailing front and the cyclone as its parent system. All other identified fronts in the NA are removed from the database at this time step, as they are not associated with a parent low and hence do not satisfy the objective criteria for cyclogenesis on a trailing front. Along the front precipitation is observed, with a maximum 6 h sum of 20 mm at 53.5°W, 43°N slightly southeast of Newfoundland. To the southwest of the precipitation maximum, a cyclogenesis is detected at 54°W, 40°N slightly ahead of the trailing front located within the pre-frontal band of precipitation. This cyclogenesis is accepted as a frontal-wave cyclogenesis. Due to the minimum advection threshold criterion applied during the front detection, and due to the requirement to attend a parent system, the identified trailing front is distinct from the zone of enhanced low-level baroclinicity over the Gulf Stream.

Turning to the second example over the eastern NA (Figure 1(b)), identified at 0600 UTC on 18 December 2013, the frontal-wave cyclogenesis is located on the northern tip of a cold front at 23°W, 51°N. This cold front decoupled from the main low several hours earlier but is still intersecting the outermost closed isobar of the parent low. A noteworthy characteristic is the short-wave trough in the sea-level isobars seen around the genesis location and, similar to the first example, a local spot of maximum precipitation (10–14 mm within 6 h). This time the frontal-wave cyclogenesis is co-located with the precipitation maximum. This example corresponds to the development on the tip of a low-level PV band as described by Appenzeller and Davies (1996) and is reminiscent of many of the previously analysed classical frontal waves in the literature. These genesis types typically constitute rapidly deepening cyclones of sub-synoptic scale. As will become clear during the course of this study, frontal-wave cyclogenesis events in the eastern NA are on average associated with more enhanced lower- and upper-tropospheric flow anomalies than cases in the western NA.

© 2015 The Authors. *Quarterly Journal of the Royal Meteorological Society* published by John Wiley & Sons Ltd on behalf of the Royal Meteorological Society.

Q. J. R. Meteorol. Soc. **141**: 2989–3005 (2015)

Figure 1. Two illustrative examples of frontal-wave cyclogenesis at (a) 0600 UTC on 29 October 1985 over the Gulf Stream region and (b) at 0600 UTC on 18 December 2013 in the eastern North Atlantic: the detected fronts (thick black solid lines), SLP contours in 10 hPa steps (thin black solid lines), detected cyclogenesis events (red crosses), 6 h accumulated precipitation (colour, mm) and wind (barbs, m s^{-1}). The parent low pressure systems are labelled L. [Correction added on 26 August 2015, after first online publication: The date and time in the text reference and caption of Figure 1 were previously wrong. These have been updated in this version.]

2.3. Analysis procedure

2.3.1. Horizontal analysis

The ambient conditions encompassing frontal-wave cyclogenesis are characterised by horizontal composites in section 4. The present composites are centred around the location of cyclogenesis and all fronts are oriented into the north−south direction to minimize the smoothing effect by variations in the orientation of the front.

To this end, a coordinate system transformation into a local domain is conducted, which rotates a virtual equator through the location of frontal-wave cyclogenesis, thereby ensuring that all grid points account for a comparable area before the composition is performed.* The rotated quasi-equidistant limited local domain covers an area of ± 10° (∼1100 km) in south−north and west−east directions. Afterwards the fronts are rotated such that they align along the north−south axis by minimizing the sum of all distances between frontal grid points and the centre meridian of the local domain. The warm side of the front is always located in the eastern part of the composite domain. A composite of all rotated fronts after this two-step procedure is shown in Appendix A), which highlights the quality of the alignment.

Several variables are analysed in section 4, for example low-level averaged PV and deformation, but also surface precipitation, dry and moist static stability and surface heat and moisture fluxes. Low-level averages are taken between the 950 and 800 hPa levels.

2.3.2. Vertical analysis

Turning to the vertical structure of frontal-wave cyclogenesis, composites of vertical cross-section are investigated in section 5. The vertical cross-sections are taken perpendicular to the trailing fronts at the location of cyclogenesis. It is ensured that the colder side of the front is located in the western part of the domain.

For the analysis of the vertical structure, the focus is given to the PV perspective, which in the past was used successfully in studies on frontogenesis (Davies and Rossa, 1998), cyclogenesis (Davis and Emanuel, 1991), life cycle assessments of individual cases (Wernli *et al.*, 2002) and climatologies Čampa and Wernli (2012). Hoskins *et al.* (1985) provide a review of PV dynamics.

2.3.3. Along-frontal stretching and deformation analysis

In order to gain insights into typical stretching and shearing tendencies of the ambient wind, a multi-decadal analysis is performed in section 6. For a two-dimensional wind field, $\mathbf{u} = (u, v)$, the deformation of the flow field is given by

$$D = \left\{ \left(\frac{\partial u}{\partial x} - \frac{\partial v}{\partial y} \right)^2 + \left(\frac{\partial u}{\partial y} + \frac{\partial v}{\partial x} \right)^2 \right\}^{1/2}, \tag{1}$$
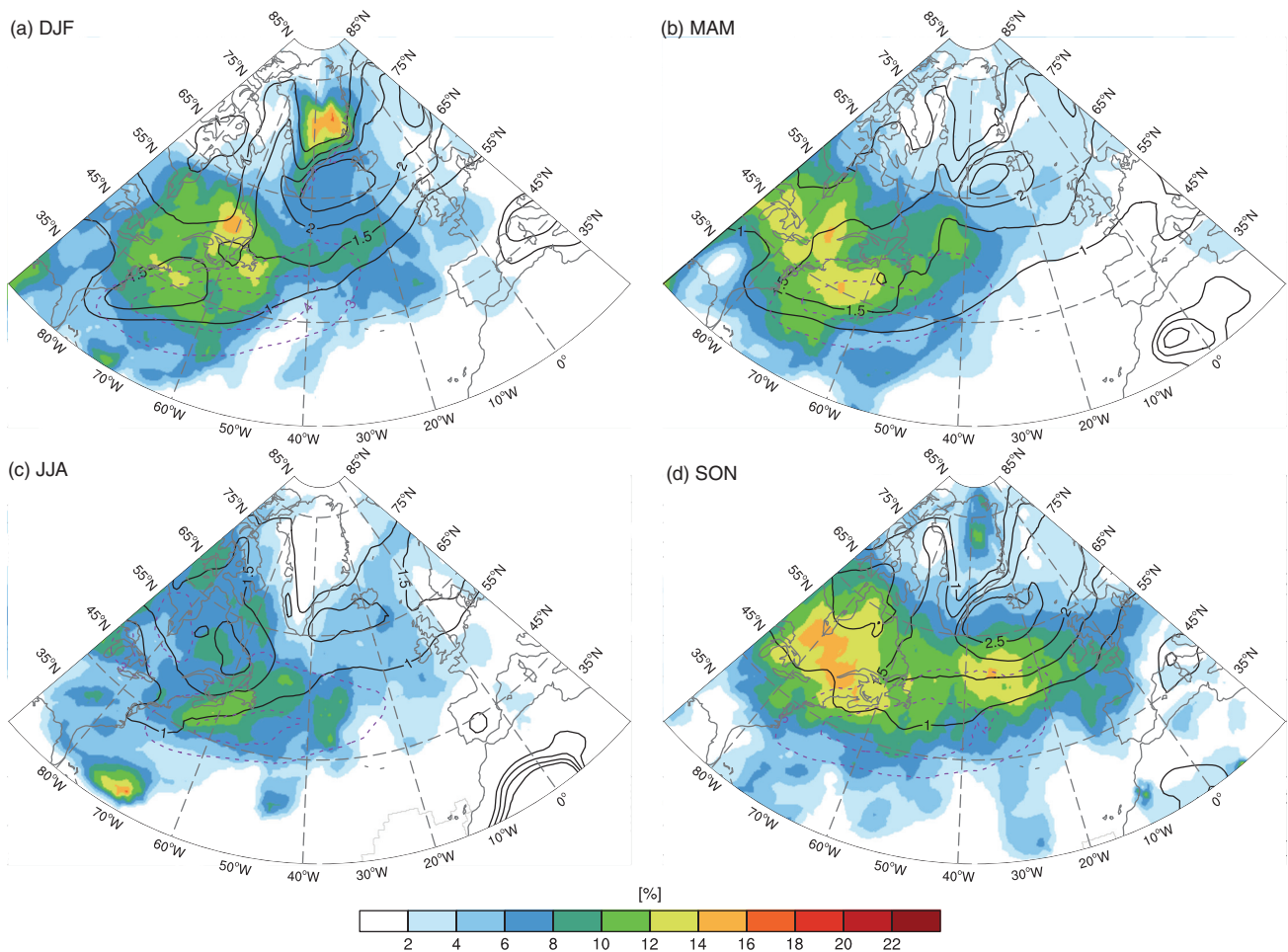
where the first component, i.e. $\partial u/\partial x - \partial v/\partial y$, represents the stretching of an air parcel, and $\partial/\partial x$ and $\partial/\partial y$ denote partial derivatives in the across- and along-frontal direction, respectively. The second component denotes the shearing of an air parcel located in the centre of the coordinate system. In general, deformation acting on an air parcel changes the shape of the fluid element by a combination of stretching and shearing along a properly chosen coordinate axis, i.e. if the front is aligned with one of the axes.

To obtain along-frontal stretching rates which can be compared to the large-scale deformation fields imposed in idealised studies or theoretical models, the observed wind field must be decomposed into an environmental and frontal-flow part. To this end, Bishop (1996a, 1996b) introduced a partition method which decomposes the wind field into a component attributable to vorticity and divergence anomalies outside of a box encompassing the front and oriented along the front ('frontal box'), and into a wind component attributable to vorticity and divergence anomalies inside this box. In this study we need to process a multitude of fronts and frontal-wave cyclogenesis events over a period from 1979 to 2014 in various synoptic situations in an automated way, therefore the method used here is more straightforward but will still '*be only slightly affected by frontal waves whose wavelength is smaller than the length of the frontal region [...] (the method will) overcome the problem of frontal waves creating local anomalies in the stretching rate.*' (Bishop, 1996b, p. 255).

Firstly it is assumed that the ambient wind is divergence-free at 850 hPa. Hence its components can be obtained using Helmholtz's theorem (e.g. Lynch, 1988) to split the horizontal wind into a irrotational and divergence-free component

$$\mathbf{u} = \nabla \chi + \mathbf{k} \times \nabla \psi, \tag{2}$$

where $\mathbf{k}$ is the unit vector in the vertical plane, ψ a streamfunction and χ the velocity potential. The divergence-free component is

---

*A similar transformation is performed by the limited-area COSMO (Steppeler *et al.*, 2003). A more detailed description of the implementation is given in Part I Section 3 of the COSMO documentation which is available at http://www.cosmo-model.org; accessed 4 June 2015.

© 2015 The Authors. *Quarterly Journal of the Royal Meteorological Society* published by John Wiley & Sons Ltd on behalf of the Royal Meteorological Society.

Q. J. R. Meteorol. Soc. **141**: 2989–3005 (2015)

Figure 2. The frontal-wave cyclogenesis fraction (%) of all cyclogenesis (colour shading) for (a) DJF, (b) MAM, (c) JJA and (d) SON. Additional contours show detection rates of cyclogenesis (black; %) and detection rates of trailing fronts (dashed purple; for 3, 4 and 5%) for the time period from 1979 to DJF 2013/2014.

taken as the ambient wind field ($\mathbf{u}_a$) needed in our study. The equation can be solved for the divergence-free component by a Poisson equation for the streamfunction: $\nabla^2 \psi = \zeta$, where ζ denotes the relative vorticity, $\zeta = \mathbf{k} \cdot \nabla \times \mathbf{u}$. The inversion is performed on a regional domain using Dirichlet boundary conditions (Lynch, 1988).

To calculate the mean stretching rate over the frontal region, recall that the detection of fronts relies on gradients in θ_e at 850 hPa. The along-frontal component of the ambient wind is

$$v_{af} = \widehat{\mathbf{n}} \cdot \mathbf{u}_a, \tag{3}$$

where $\mathbf{u}_a$ is the ambient (divergence-free) wind obtained from Eq. (2), and $\widehat{\mathbf{n}} = \mathbf{k} \times \nabla \theta_e / |\nabla \theta_e|$ denotes the unit vector in the along-frontal direction. In practice the θ_e field at 850 hPa is smoothed several times to obtain a robust result for the along-frontal unit vector. The along-frontal stretching of the ambient wind is then obtained by taking the derivative parallel to the frontal zone, i.e.

$$\frac{\partial v_{af}}{\partial y_f} = \widehat{\mathbf{n}} \cdot \nabla v_{af}. \tag{4}$$

In the following the subscript f which denotes the along-front direction is omitted and we refer to $\partial v_a / \partial y$ as the along-frontal stretching component of the ambient wind.

Finally one characteristic along-frontal stretching rate is assigned to every front. It is obtained as an average over the entire front.

3. Seasonal climatologies of frontal-wave cyclogenesis

It is pertinent to start the analysis with a discussion on the obtained climatology of frontal-wave cyclogenesis. The

climatology (Figure 2) shows the detection rates of cyclogenesis (black solid), of trailing fronts (purple dashed) and the proportion of frontal-wave cyclogenesis (colour). The detection rates or detection frequencies are obtained by a time average of binary fields over all time steps in one season. The binary fields are obtained by setting all grid-points inside the cyclone's closed isobar (at genesis) to 1, and areas outside to zero. A similar procedure is done for all trailing fronts (as outlined in section 2). Thereafter a time average yields a detection rate at each grid-point per chosen time window, e.g. the winter season. For instance, a detection rate of 1% means that, on average, in 1 out of 100 time steps, a feature, e.g. a trailing front, is detected. The proportion is the fraction of two detection rates, i.e. detection rates of frontal-wave cyclogenesis divided by detection rates of all cyclogenesis events. Note that frontal-wave development rarely occurs on warm fronts and the presented climatology encompasses frontal-wave cyclogenesis on all types of front, i.e. cold, warm and occluded fronts.

During the winter season (DJF) two cyclogenesis maxima are apparent in the NA (Figure 2(a)). The first is located in the western NA with a clear maximum in the Gulf Stream region (1.5%). The second maximum is identified at the southeastern tip of Greenland (>2.5%). Another, albeit weaker, maximum (~1%) is found north of Hudson Bay at 79°W, 64°N. The DJF climatology of trailing fronts is mostly confined to the main storm-track region, extending from the Gulf Stream region eastward into the central NA. It agrees well with the front climatology of Schemm *et al.* (2014). Outside of the main storm tracks, along the southeastern coastline of Greenland, trailing fronts are identified at 3% of all DJF time steps.

The proportion of frontal-wave cyclogenesis amounts to up to 8–10% in a wider region spanning from Hudson Bay in the north, to the Great Lakes in the east over the Gulf Stream region

© 2015 The Authors. *Quarterly Journal of the Royal Meteorological Society* published by John Wiley & Sons Ltd on behalf of the Royal Meteorological Society.

Q. J. R. Meteorol. Soc. **141**: 2989–3005 (2015)

and further east into the central NA to 25°W, 54°. Within this broader area, several distinct locations with enhanced values are observable. For example, to the east of Cape Cod and east of Newfoundland, frontal-wave cyclogenesis accounts for ∼12–14% of all genesis events and in Québec and the Labrador/Newfoundland region the proportion increases to up to 14–16%. Along the European Atlantic coast around 4–6% of all genesis events are identified on trailing fronts and classified accordingly.

The enhanced relative contribution of frontal-wave cyclogenesis over Greenland is noteworthy. The cases in this region might not fall into the archetypal category of frontal-wave cyclogenesis, but are associated with fronts detected along the southeastern coast of Greenland and low pressure systems developing in this area. Later in the analyses of horizontal and vertical cross-sections, frontal-wave cyclogenesis in polar latitudes is excluded from the sample list.

During spring (MAM; Figure 2(b)) the proportion of frontal-wave cyclogenesis and the climatology of trailing fronts extend less into the eastern NA and are more confined to the Gulf Stream area. From the Gulf Stream westward to the Great Lakes, frontal-wave cyclogenesis accounts for up to 14–16% of all genesis cases. In general the values for the detection rates of trailing fronts, cyclogenesis and the relative frequencies of frontal-wave cyclogenesis remain comparable to DJF rates. Besides the retreat of the pattern from the eastern NA, the major difference from DJF is observed along Greenland, where the proportion of frontal-wave cyclogenesis (2% of all cyclogenesis) and the detection rates of trailing fronts (<1%) reduce strongly.

Significant changes occur during the summer season (JJA) shown in Figure 2(c). Cyclogenesis is shifted to higher latitudes with two identified maxima north of 45°N – one located over Québec and a second one between Greenland and Iceland, with cyclogenesis detected at 2% of all time steps. Likewise the trailing fronts have shifted poleward and their climatology extends further eastward than in DJF, i.e. detecting rates of 3% are still identified at 22°W, 45°N which is not the case during DJF. However frontal-wave cyclogenesis is hardly detected in the summer months over the eastern NA, i.e. only 2–4% of all cyclogenesis cases are on a trailing front. The proportion is highest in the western NA east of Nova Scotia (8–10%) and in the central NA at 38°W, 43°N where the fraction of frontal-wave cyclogenesis is 10%. Note that the local maximum in proportion east of Florida at 70°W, 26° during JJA relates to systems developing in the subtropical belt of the western NA on strong fronts driven by enhanced humidity gradients. We do not consider the identified cases in this small area as classical frontal-wave cyclogenesis.

Finally, during autumn (SON; Figure 2(d)) the detection rates of frontal-wave cyclogenesis start to increase again over the whole NA. In particular in an area encompassing the Great Lakes and Hudson Bay and further to the east towards Newfoundland and into the central NA (∼10–15% of all cyclogenesis). A second strong maximum of frontal-wave cyclogenesis (∼15%) is located in the eastern NA at 38°W, 54°N, located south of the major cyclogenesis maximum between Greenland and Iceland. Cyclones which develop on frontal waves in this area typically propagate eastward towards Europe and are associated with high-impact weather (Parker, 1998). Along the European Atlantic coast, frontal-wave cyclogenesis during SON is much more frequent than in any other season (e.g. 4–5% more than during DJF). Likely frontal-wave cyclogenesis occurs in the central NA on cold fronts which are trailing low pressure systems originating from the southeastern tip of Greenland. Note again that cases in polar latitudes are excluded from further analysis.

4. Horizontal composite analysis: characterisation of environmental conditions

Further insights into the nature of the ambient flow can be gained if frontal-wave cyclogenesis is examined separately for the western (80 to 41°W, 25–50°N) and eastern (39 to 0°W, 35–60°N) NA basins. The horizontal composites show the mean value over all samples and the standard deviation (σ) over the input sample (calculated at the location of genesis) is shown on each panel. Recall that all fronts are oriented into the north–south direction.
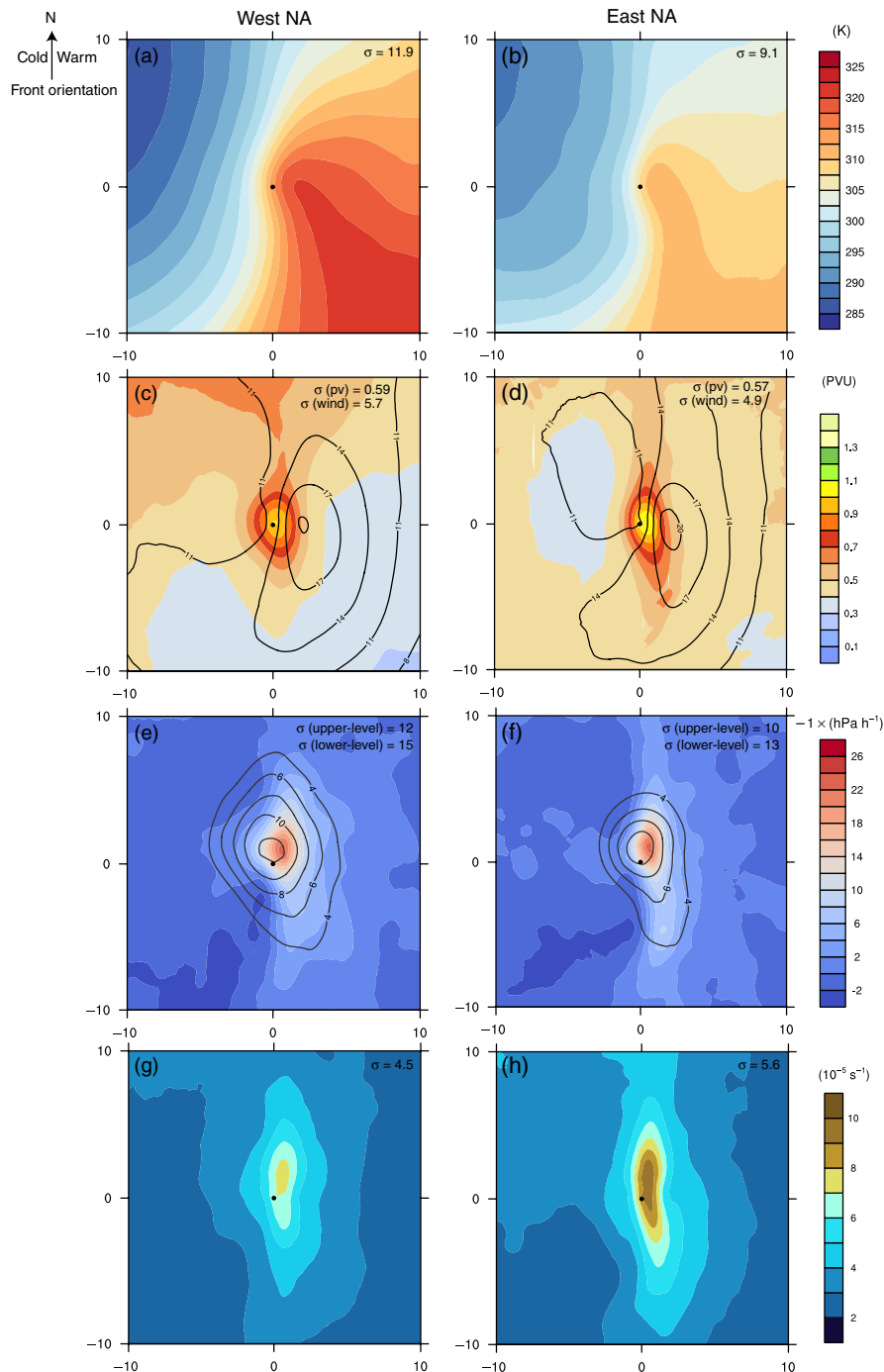
4.1. Frontal strength

The composites reveal differences between frontal-wave cyclogenesis in the two basins: in the western NA (Figure 3(a)), θ_e at 850 hPa appears to be higher on the warmer side of the front by up to 8–10 K and slightly lower on the colder side of the front (by around 1 K). This results in an enhanced across-frontal gradient in the western NA and hence fronts are on average stronger in this basin. The variability in the western NA is slightly higher with σ values of around 12 K compared to 9 K in the eastern NA. Hence frontal-wave cyclogenesis occurs typically on stronger fronts in the western NA, which can be expected since θ_e gradients are climatologically higher in the western NA over the Gulf Stream. In particular the developing warm front is much weaker in the eastern NA. The composed pattern of θ_e depicts the early development stage of a cyclone's warm sector. In the eastern NA (Figure 3(b)), we find a narrower warm sector with a distinct and banded positive anomaly of θ_e alongside the front. This warm anomaly is reminiscent of the warm frontal band in the analytical model of Schär and Davies (1990) imposed ahead of the cold front.

4.2. PV, wind speed, omega and deformation

Turning to PV, Figure 3(c,d) show low-level averaged (950 to 800 hPa) PV. In both basins a clear signal of enhanced low-level PV is observable at the location of cyclogenesis in the centre of the domain. While in the western NA PV reaches up to 0.9–1.0 pvu, PV values in the east NA are higher, with mean values around 1.0–1.1 pvu, and spread over a wider area. The variability of the sample around the cyclogenesis location is only marginally higher in the western NA ($\sigma = 0.59$ pvu compared to 0.57 pvu in the eastern NA). The pattern in the eastern NA, in particular the 0.6 pvu contour, reveals the elongated along-frontal PV band assumed in the theoretical analysis of Joly and Thorpe (1990). In the western NA the PV band is less pronounced. Horizontal PV gradients appear to be stronger in the eastern NA, which suggests enhanced along-frontal wind (black contours) during the developments. Note that the mean low-level PV values in the eastern NA is contained within the range of $\overline{PV}_{\text{west NA}} \pm \sigma(PV_{\text{west NA}})$ and vice versa (the bar denotes the sample mean). Hence the differences cannot be denoted as systematic. Nevertheless higher mean low-level PV and gradients suggest higher vertical updraughts by enhanced column stretching and wind speed.

Isotachs of low-level averaged wind (Figure 3(c,d)) reveal higher wind speed on the warmer side of the front by almost a factor of 2 than on the colder side. In the eastern NA, wind speed on the warmer side of the front is slightly higher by ∼1–2 m s^{-1} than in the western NA, as suggested by the PV gradients. However the mean values at the precise location of genesis differ only marginally between the two basins (∼11 m s^{-1}).

Low-level averaged vertical motion ω (hPa h^{-1}) is presented in Figure 3(e,f), together with upper-level (400 to 300 hPa) averaged ω. Note that the sign convention has been reversed, such that positive values indicate upward motion. In the western NA (Figure 3(e)) maximum low-level updraughts are in the order of 20 hPa h^{-1} and are situated slightly to the northeast of the minimum SLP. In the eastern NA, strongest vertical motion in the lower troposphere is in the same order of magnitude (∼ 20 hPa h^{-1}) and again maximum values are found to the northeast of the genesis location. The variability of the sample is similar,

ⓒ 2015 The Authors. *Quarterly Journal of the Royal Meteorological Society* published by John Wiley & Sons Ltd on behalf of the Royal Meteorological Society.
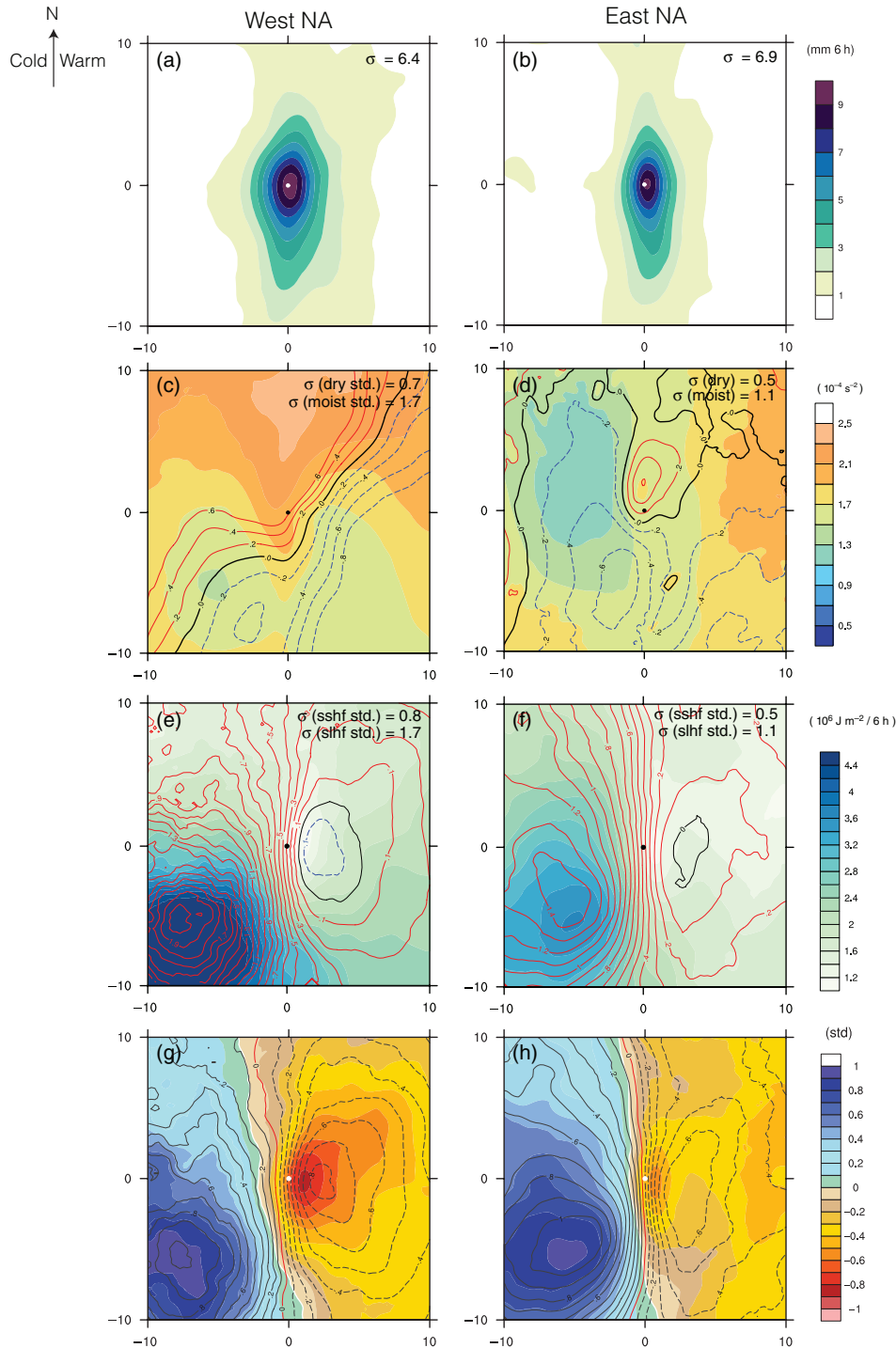
Q. J. R. Meteorol. Soc. **141**: 2989–3005 (2015)

Figure 3. Horizontal composites and the sample standard deviation (σ) centred at frontal-wave cyclogenesis in (a,c,e,g) the western NA and (b,d,f,h) the eastern NA. All fronts are rotated into the north–south direction. (a,b) Equivalent potential temperature (K; colour) at 850 hPa, (c,d) low-level averaged (950 to 800 hPa) potential vorticity (pvu; colour) and wind speed from 8 to 20 in steps of 3 m s^{-1} (contours), (e,f) low-level (950 to 800 hPa; colour) and upper-level (400 to 300 hPa; contours) averaged ω (hPa h^{-1}), and (g,h) low-level averaged deformation (10^{-5} s^{-1}; colour). The total number of composite samples in the western (eastern) NA is 207 (125).

with $\sigma = 13$ hPa h^{-1} in the eastern NA and $\sigma = 15$ hPa h^{-1} in the western NA. Both basins bear strong similarities for ω in the lower troposphere in contrast to the upper troposphere. Note that the ω signal is composed of the frontal cyclogenesis and the frontal circulation. Hence the effect of the strain on the frontal circulation, which partially acts independently of the frontal cyclogenesis, might be of different strength in the two basins.

At upper levels vertical motion reaches up to 12 hPa h^{-1} in the western NA, higher than in the eastern NA (10 hPa h^{-1}). Note that the strongest vertical motion at upper levels is located to the north of the cyclogenesis position at the surface, while strongest vertical motion at lower levels is identified to the northeast. This probably anticipates the direction of travel of the developing system. The standard deviation (σ) at upper and lower levels is higher for the western NA by around 2 K. Noteworthy is the different strength of upper- and lower-tropospheric ω in both basins. Whilst low-level

ω is comparable in the eastern and western NA, upper-level ω is stronger in the western NA by ~2 hPa h^{-1}. However we note that the box defining the eastern NA is shifted by 10° poleward relative to the western NA box. Accordingly the mean height of the tropopause is lower in the eastern NA (as shown below in Figure 5) and the strongest updraughts might not be located within the same vertical pressure layer as in the western NA (recall for Figure 3(e,f) that upper-level ω is averaged between 400 and 300 hPa). A detailed **Q**-vector analysis may prove useful in the assessment of vertical motion. To shed some light on the vertical distribution of the updraughts, the height of the tropopause and the vertical structure of PV, we discuss vertical cross-sections in more detail in section 5.

So far we find stronger (averaged) lower-tropospheric PV values and horizontal PV gradients in the eastern NA. However, vertical motion in the lower troposphere is comparable in the

© 2015 The Authors. *Quarterly Journal of the Royal Meteorological Society* published by John Wiley & Sons Ltd on behalf of the Royal Meteorological Society.

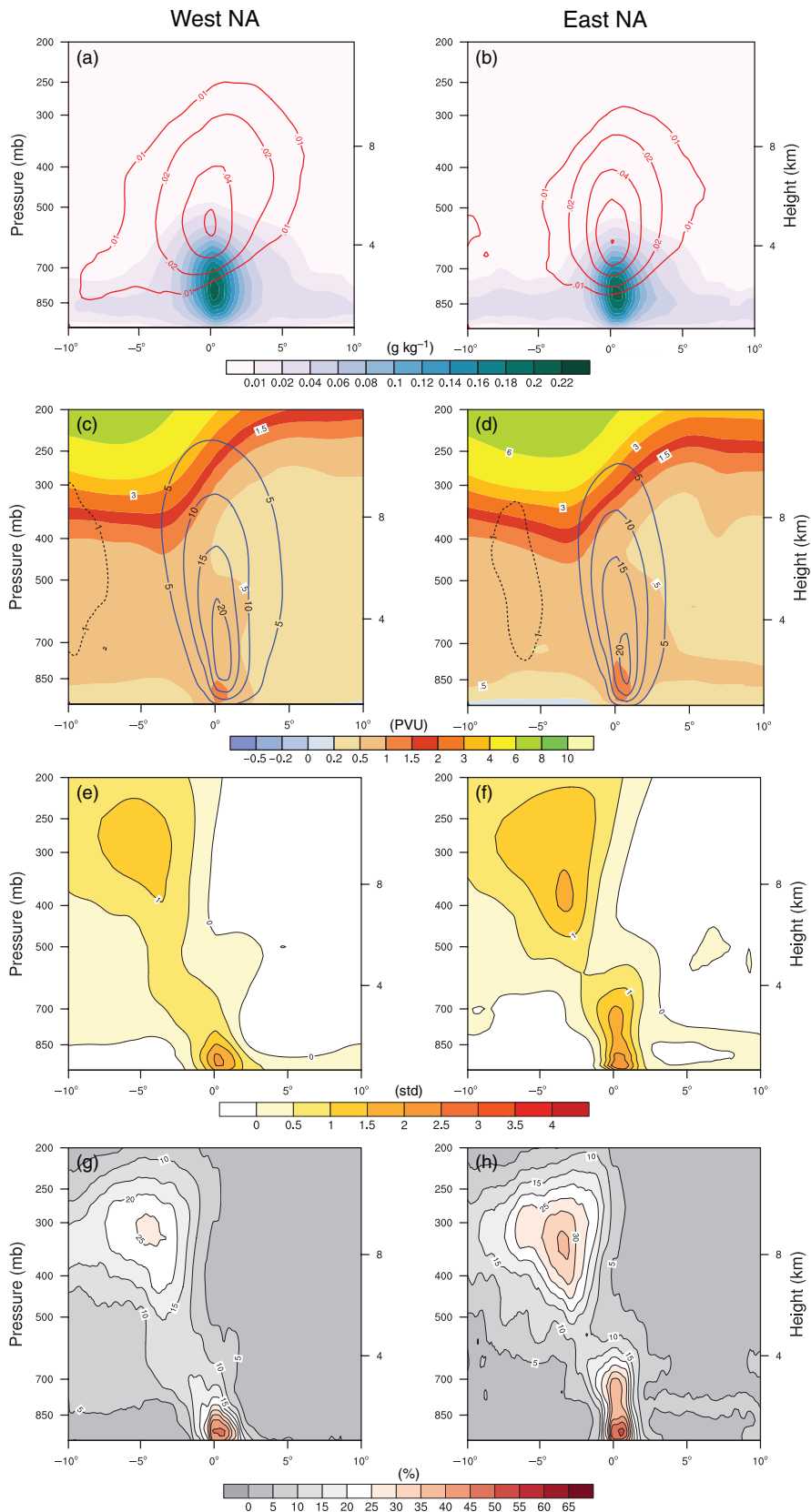*Q. J. R. Meteorol. Soc.* **141**: 2989–3005 (2015)

Figure 4. As Figure 3, but showing (a,b) 6 h accumulated precipitation (mm), (c,d) low-level averaged (950 to 800 hPa) dry (colour) and moist (red contours positive, blue contours negative values) static stability (10^{-4} s^{-2}), (e,f) 6 h accumulated surface sensible (red contours positive, blue contours negative values) and latent heat flux (colour) with positive flux directed upwards (10^{6} J m^{-2}), and (g,h) standardised surface flux anomalies. Total number of composite members in western (eastern) NA is 207 (125).

two basins. Assuming cyclonic vorticity tendencies to be stronger in the eastern NA, enhanced column stretching would result in stronger vertical motion. A stronger damping of vertical motion in the eastern NA might be attributed to stronger stretching rates (Figure 3(g,h)). As discussed in the Introduction, along-frontal stretching rates weaken and suppress the frontal-wave growth which ultimately also reduces vertical motion. The comparison between the two basins reveals stronger deformation rates for frontal waves in the eastern NA with 9×10^{-5} s^{-1} compared to 7×10^{-5} s^{-1} in the western NA. In section 6 we discuss the role of along-frontal stretching in greater detail. Note that the variability of the two samples at the location of cyclogenesis does not differ strongly ($\sigma = 4 \times 10^{-5}$ s^{-1} for both samples).

4.3.   Precipitation, dry and moist static stability

Looking at 6 h accumulated precipitation sums (Figure 4(a,b)), we find on average 10 mm in the western NA i.e. slightly higher value (by ~1 mm) than in the eastern NA. Since at the location of genesis the standard deviations of both samples are of similar order ($\sigma = $ ~6−7), precipitation rates during frontal-wave cyclogenesis are not systematically different between the two basins. Taking pre-frontal rain formation as a proxy for diabatic PV modification (as in the conceptual model of frontal-wave development introduced earlier) and since both basins show similar precipitation rates, higher low-level PV values in the eastern NA (Figure 3(c,d)) can be a result of higher vertical gradients of the heating rate tendency. PV increases

ⓒ 2015 The Authors. *Quarterly Journal of the Royal Meteorological Society*
published by John Wiley & Sons Ltd on behalf of the Royal Meteorological Society.

Q. J. R. Meteorol. Soc. **141**: 2989−3005 (2015)

Figure 5. Composites of vertical cross-sections in the across-front direction at frontal-wave cyclogenesis in (a,c,e,g) the western and (b,d,f,h) eastern NA for (a,b) liquid (blue contours) and ice water (red contours) content (g kg^{-1}), (c,d) PV (pvu; colour) and ω (hPa h^{-1}; contours, negative dashed), (e,f) standardised seasonal PV anomalies (std), and (g,h) percentage of events with a standardised seasonal PV anomalies greater than 2 std.

are proportional to vertical gradients of latent heating rates in the strongly rising motion along the front, e.g. the warm conveyor belt (Eliassen and Kleinschmied, 1957; Wernli and Davies, 1997). Below the maximum of latent heat release, positive PV anomalies are induced in the air moving along the front, e.g. the cold conveyor belt (Schemm and Wernli, 2014). Beyond this, systematic differences in low-level stability, surface fluxes or

friction acting along the strong frontal zones (Stoelinga, 1996) can add to the observed low-level PV differences between the two basins. In the following section we analyse stability and surface fluxes in greater detail.

Figure 4(c,d) show low-level averaged dry and moist static stability and σ for both at cyclo-genesis. Dry and moist static stability are defined as $N^2(\theta) = (g/\theta)\,\partial\theta/\partial z$ and $N^2(\theta_e) =$

© 2015 The Authors. *Quarterly Journal of the Royal Meteorological Society* published by John Wiley & Sons Ltd on behalf of the Royal Meteorological Society.

Q. J. R. Meteorol. Soc. **141**: 2989–3005 (2015)

$(g/\theta_e)\,\partial\theta_e/\partial z$, respectively. In the western NA frontal-wave cyclogenesis is detected in an absolutely stable environment. However it is seen slightly to the north of a broader zone where the lower-tropospheric layer is potentially unstable. The pattern of dry and moist static stability in the western NA is dominated by the background climatology maintained by ocean fluxes above the Gulf Stream. Characteristic is the elongated transition zone from potentially to absolutely stable conditions, located above a strong sea surface temperature front. Clearly noticeable however is a undulation in the dry static stability pattern of the frontal wave. Hence air parcels which move along the surface front are conditionally unstable and in case of saturation, e.g. due to moisture uptake from the ocean surface and adiabatic cooling during the slantwise ascent along the surface front, can immediately ascend until they reach a new equilibrium.

In the eastern NA (Figure 4(d)) the situation is less determined by the underlying climatology. To the north of the identified frontal-wave cyclogenesis, large areas show moderate dry static stability $(1.4 \times 10^{-4}\,\mathrm{s}^{-2})$ and are absolutely stable. The lower tropospheric layers to the south and west of the frontal wave (mostly the colder side of the front) are potentially unstable. The genesis location is identified close to a zone which is fairly neutral to moist convection $(N(\theta_e)^2 \sim 0)$. Frontal-wave cyclogenesis in the western NA is located slightly further to the north of the zone of neutral moist static stability. We assume this to be a consequence of the time required to form the first closed sea-level isobar (which is detected by the cyclone identification scheme) after the onset of cyclogenesis along the zone of neutral stability. Neutrality to moist convection is assumed by Bishop and Thorpe (1994a) in their idealised setting of frontal-wave growth and hence is proven by the composites to be a reasonable assumption. Emanuel *et al.* (1987) showed that the fastest growing mode in environments that are neutral to slantwise moist convection is up to 2.5 times higher than dry growth rates. Additionally cyclone scales are reduced by a factor of 0.6 compared to a dry wave. The model of Emanuel *et al.* (1987) also assumes no along-frontal variability, but still produces an along-frontal precipitation band.

Low-level dry and moist static stability are on average higher than in the eastern NA by $0.4-0.6 \times 10^{-4}\,\mathrm{s}^{-2}$, and the mean values from the eastern NA are clearly outside the standard deviation of the western NA, suggesting a systematic difference. Overall the findings suggest that the ambient atmospheric conditions for an air parcel moving along the front prior to frontal-wave cyclogenesis are conditionally unstable prior to the detection of the first closed sea-level isobar. The instability is released during genesis and, after the formation of the first closed sea-level isobar, cyclogenesis is identified in an absolutely stable environment.

Figure B1 presents cross-sections for relative humidity which are of interest for the design of future idealised experiments. The low-level averaged relative humidity field reveals saturation (90–95%) at cyclogenesis in a broader zone along the front. Appenzeller and Davies (1996) in their frontal-wave case-study find relative humidity value of around 90% in the lower troposphere. Within a distance of around 500 km in the across-frontal direction, the ambient air still shows relative humidity values of ∼70% (with a standard deviation of ∼10%). In the vertical, relative humidity decreases steadily from saturation to around 80% at 700 hPa and 60% at 500 hPa. Hence the assumption in the idealised frontal-wave model of Bishop and Thorpe (1994a) of saturated ambient air holds true for the lower troposphere.

4.4.   Surface fluxes

Finally we complete the horizontal characterisation of ambient conditions during cyclogenesis on fronts by considering sensible and latent heat fluxes from ocean grid-points. The composites of 6 h accumulated sensible and latent heat fluxes are presented in Figure 4(e,f) for the western and eastern NA. It is important to note the sign convention of the fluxes. Positive fluxes are oriented upward in this study, consequently positive flux indicates heat and moisture transfer into the atmosphere. Moisture gain by the air is indicated by bluish colours in the composite figures and heat input into the atmosphere by red contours.

Sensible fluxes are predominantly positive during frontal cyclogenesis in both basins. However, a minor region to the east of the precise genesis location indicates negative values in the western NA (note the zero contour which is highlighted in black, Figure 4(e)). This is associated with heat loss of the atmosphere due to the advection of warmer air along the surface front which, if the advected air is warmer than the ocean surface, causes a cooling.

Latent heat transport appears to be positive but weak around the genesis location, as all air parcels are probably saturated or close to saturation, unlike the colder side of the front, where strong positive upward latent flux indicates evaporation from the ocean into predominantly cold and dry air. Overall the findings also apply to the eastern NA (Figure 4(f)), although the pattern is weaker, except around the genesis location.

Standardised and seasonally averaged flux anomalies for both basins are presented in Figure 4(g,h). Standardised anomalies are defined as the deviation from the respective seasonal climatology and are divided by the seasonal standard deviation at each grid-point. Negative anomalies indicate less uptake of heat and moisture than in the climatological mean, which is typically directed into the atmosphere (positive). More moisture uptake than average is shown in blue, and less in red. Dashed contours indicate less heating than average. The eastern NA reveals a location shift of the flux anomalies on the warmer side of the front, i.e. strongest anomalies of sensible heat flux are not found at the same location as latent heat flux. The strongest sensible heat flux anomaly is located further southeast than the flux anomaly of latent heat. Hence an air parcel that is advected northwards along the front receives less heating from the ocean than average or is even cooled. Accordingly the saturation deficit decreases, i.e. the air is getting closer to saturation, and evaporation from the surface is steadily reduced. As a consequence, the negative latent heat flux anomaly, i.e. less moisture uptake than average, occurs to the north of the sensible heat flux anomaly. At the same time as moving along the warmer side of the front, buoyancy increases due to the moisture uptake and, as soon as saturation occurs, latent heat propels the ascent. This most likely occurs on the warmer side of the front, thus the strongest negative latent heat flux anomaly (less moistening, hence red colours) is observed closer to the genesis location.

In contrast to this, behind the cold front, both flux anomalies are positive in the eastern and western NA, i.e. heat/moisture uptakes are higher than average. Both transport anomalies are in a similar range ($\sim 1\,\sigma$) and are found at a comparable location.

To summarise briefly the differences between surface fluxes in the two basins, we note that the amplitudes of the anomalies differ between the western and eastern NA. Sensible heat flux anomalies in the eastern NA are weaker on the warmer side of the front, i.e. closer to the climatological mean. This indicates less heat uptake of the atmosphere in the eastern NA than in the western NA. Similarly, a weaker negative latent heat flux anomaly in the eastern NA indicates less moisture uptake than in the western NA compared with the respective ocal climatology. In other words, air parcels in the eastern NA are closer to saturation.

5.   Vertical composite analysis: PV cross-sections and water content

As stated in the Introduction, the mutual interaction and amplification of the lower- and upper-tropospheric waves are crucial for the continuous deepening of the system and its translation into a baroclinic depression. To shed light on the intensity and shape of the upper-level forcing and the vertical structure, we now turn

to consider PV and ω in vertical across-frontal cross-sections. Furthermore, to obtain insight into diabatic modifications, we also present corresponding composites for liquid and ice water content. As in the foregoing sections, western NA cases are treated independently from eastern NA cases (Figure 5).

Firstly we present cross-sections of liquid and ice water content taken in the across-front direction (Figure 5(a,b)). Liquid water content is mostly confined to the lower troposphere at around 800 hPa, where both composites show around $0.2\,\mathrm{g\,kg^{-1}}$ of liquid water. The sample variation is slightly higher in the western NA, but overall the liquid water content is in a similar range for both basins. However liquid water extends deeper into the mid-troposphere in the western NA, e.g. $1\times10^{-3}\,\mathrm{g\,kg^{-1}}$ is observable at 500 hPa which is not the case in the eastern NA. Stronger differences are observed in ice water content. Again the absolute values are comparable ($6\times10^{-3}\,\mathrm{g\,kg^{-1}}$ at 550 hPa), but in the western NA ice clouds reach deeper into the upper troposphere. We find on average $1\times10^{-3}\,\mathrm{g\,kg^{-1}}$ of ice at 250 hPa in the western NA, but this value at around 300 hPa in the eastern NA. The difference is not strongly pronounced, but it is key to the differences in upper-tropospheric ω, which we discussed earlier. We come back to this in the discussion of the PV cross-sections below.

The vertical cross-sections of PV in the across-front direction together with ω for the two basins are presented in Figure 5(c,d). In both, a pronounced and locally confined strong PV signal of around 1–1.5 pvu is observable at lower levels. A noticeable difference close to the surface is a region of relatively weak PV values (0–0.2 pvu, blue colours) located behind the cold front in the eastern NA (Figure 5(d)). This characteristic is absent in the western NA (Figure 5(c)). As a consequence, the cross-frontal PV gradient is stronger, as already noted earlier. The associated wind speed can be expected to be higher and the local pressure gradients stronger. The lower-level PV anomaly of 1 pvu reaches deeper into the troposphere in the eastern NA. In the upper troposphere, the vertical cross-sections in both basins display a trough signal. The dynamical tropopause (2 pvu, red) slants down to 380–400 hPa in the eastern NA. In the western NA, the tropopause is located slightly higher (350 hPa). The PV cross-section in the across-front direction bears close similarities to the cross-section obtained in the frontal-wave case study by Appenzeller and Davies (1996). In their eastern NA case-study, the dynamical tropopause slants down to 500 hPa and the westward shift with height between the top and surface anomaly is approximately 600 km. The westward shift with height of the frontal PV maximum and the upper-level PV trough is approximately $\sim$350 km in the eastern and $\sim$450 km in the western NA. The difference in the shift compared to the findings of Appenzeller and Davies (1996) are explained by the different time of the cross-section, which is taken earlier in Appenzeller and Davies (1996).

Turning to vertical motion (blue contours) average updrafts of $20\,\mathrm{hPa\,h^{-1}}$ at 800 hPa extend up to 600 hPa in the western NA but are more confined to lower levels in the eastern NA. Likewise at the tropopause level and above, vertical motion is stronger in the layer between 400 and 300 hPa, as already discussed earlier. Accordingly the strength of the lower-level PV anomaly does not allow a conclusion on the strength of the vertical motion. So far the findings suggest that vertical motion in the eastern NA is damped along the front by higher deformation rates (as discussed in section 4.2), while in the western NA updraughts are accelerated in the mid-troposphere by latent heat released during the formation of ice.

Next the seasonal PV anomalies are divided by the seasonal standard deviation of the respective climatology at each location (Figure 5(e,f)). The thereby normalised PV anomalies are in both basins at the surface in the order of 2–2.5 standard deviations (std). At the tropopause height the composites show standardised PV anomalies of around $\sim$1.5 std in the eastern and 1 std in the western NA. Hence upper-level PV anomalies are climatologically weaker than their counterpart at the surface front. Note how in the
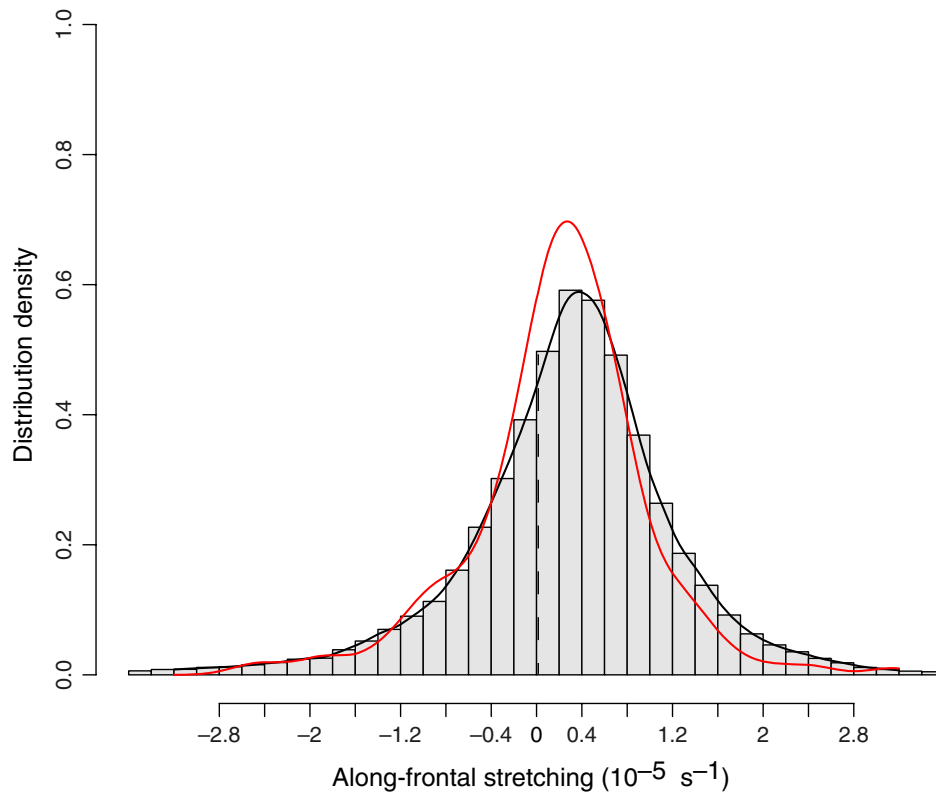
eastern NA the standardised anomaly in the order of 1 std reaches through almost the entire troposphere. By normalising the PV anomaly with the local standard deviation of the climatology, it becomes clear that the low-level PV signal during frontal-wave cyclogenesis outweighs the upper-level PV anomaly. The vertical alignment of the upper- and lower-level anomaly in the eastern NA has a weaker westward tilt with height, i.e. it is more upright than in the western NA and reaches significantly deeper into the mid-troposphere. This can be seen from the centre of the 1 std PV anomaly in the western NA which is located 5° to the west of the genesis, while in the eastern NA the centre of the 1.5 std PV anomaly is around 3° to the west of the genesis location. The PV profile in the eastern NA appears as what typically is referred to as a PV tower. In the eastern NA the phase-lock of the two anomalies is more advanced, and from the conceptual model of frontal-wave cyclogenesis this suggests that this stronger interaction between the two waves is required for the growth of the wave to overcome the stronger deformation rates in the eastern NA than in the western NA.

Figure 5(g,h) illustrate the percentage of cases with seasonal PV anomalies greater than 2 std in the samples. For the events in the western NA, 25% of all frontal-wave cyclogenesis reach anomalies above 2 std in the upper troposphere, whereas at the surface more than 45% reach this threshold. In comparison, we find in the eastern NA 40% of all frontal-wave cyclogenesis to be associated with an upper-level PV anomaly above 2 std, and at the surface front 55% of all anomalies above this value. This highlights the strength of the diabatically generated PV during frontal-wave cyclogenesis.

As a preliminary summary to the analysis of vertical PV cross-sections, we note that standardised PV anomalies greater than 2 std occur at the surface front more frequently in the eastern NA than in the western NA. Vertical motion in the mid- and upper-troposphere is on average stronger in the western NA. Intensified updraughts are also reflected in higher ice water contents in the western NA. Overall the vertical PV structure in the eastern NA shows a stronger vertical alignment of the upper- and lower-level PV anomalies. In addition both anomalies reach deeper into the mid-troposphere in the eastern NA, reminiscent of a PV tower. Recall that the presence and phase-lock of an upper-level anomaly has been described in previous studies as a key requirement for the amplification and the continuing growth of a frontal wave. Since deformation rates along the fronts are higher for frontal waves in the eastern NA, the presence of an enhanced PV anomaly at the tropopause level seems to support the growth of the frontal wave which needs to overcome the flattening tendencies imposed by along-frontal stretching. Very likely the enhanced upper-level anomaly also explains the rapid intensification of frontal-wave cyclones which is observed in the eastern NA (Parker, 1998). Note that our definition used for cyclogenesis, i.e. the occurrence of the first closed sea-level isobar for a cyclone with minimum lifetime of 24 h, ensures that all considered cases indeed overcome the transformation into a baroclinic system, and likewise frontal waves in the analysed sample phase-lock with the upper-level anomaly.

6. Along-frontal stretching and shearing deformation of the ambient wind

Stretching rates play a decisive role during the life cycle of a frontal wave. Initially they support the diabatic growth of the along-frontal PV band by strengthening vertical motion via the ageostrophic secondary circulation. Thereafter they can suppress frontal-wave growth by flattening the front. However wave suppression can also happen at the same time as the formation of the PV band. As outlined in greater detail in the Introduction, several previous studies have suggested the existence of an upper threshold for along-frontal stretching rates. Above this threshold frontal-wave growth is strongly

© 2015 The Authors. *Quarterly Journal of the Royal Meteorological Society* published by John Wiley & Sons Ltd on behalf of the Royal Meteorological Society.

Q. J. R. Meteorol. Soc. **141**: 2989–3005 (2015)

Figure 6. Histogram of along-frontal stretching rates in the North Atlantic along all trailing fronts (combined for the eastern and western NA boxes). Gaussian density estimate for all trailing fronts (black) and for trailing fronts with frontal-wave cyclogenesis on them (red). Cases over land or near continental surfaces are neglected. Note the steeper decrease for fronts with cyclogenesis (red) at rates above $0.6-0.8 \times 10^{-5}$ s^{-1}.

Table 1. Proportion (%) of frontal waves with cyclogenesis compared to all (trailing) fronts as a function of along-frontal stretching (combined for the eastern and western NA box, with frontal grid points over land removed). Bold figures are discussed in the text.

Stretching (10^{-5} s^{-1})	(%)	Stretching (10^{-5} s^{-1})	(%)
−2.0 to −1.8	0.65	0.0 to 0.2	**0.43**
−1.8 to −1.6	0.21	0.2 to 0.4	**0.43**
−1.6 to −1.4	0.16	0.4 to 0.6	**0.35**
−1.4 to −1.2	0.24	0.6 to 0.8	0.30
−1.2 to −1.0	0.46	0.8 to 1.0	0.20
−1.0 to −0.8	0.44	1.0 to 1.2	0.22
−0.8 to −0.6	0.31	1.2 to 1.4	0.22
−0.6 to −0.4	0.18	1.4 to 1.6	0.18
−0.4 to −0.2	0.38	1.6 to 1.8	0.18
−0.2 to 0.0	0.38	1.8 to 2.0	0.13

suppressed. Accordingly it is of further interest to examine along-frontal stretching climatologically and to quantify this threshold empirically. The detailed procedure to obtain the along-frontal stretching rate is introduced in section 2.3.3.

We consider first the distribution of along-frontal stretching in the NA for all trailing fronts and compare it to the distribution of all trailing fronts with frontal cyclogenesis. The former is shown in Figure 6 and reveals a Gaussian shape centred around 0.4×10^{-5} s^{-1}. Maximum values rarely exceed 3.8×10^{-5} s^{-1} and are omitted in Figure 6. For fronts with frontal-wave cyclogenesis, the distribution bears strong similarities with the full distribution. However clearly observable is a reduction of cases with stretching rates above 0.7×10^{-5} s^{-1}, where the distribution of strain rates on frontal wave with cyclogenesis decreases more strongly than in the full distribution. Overall the majority of cases develop with along-frontal stretching rates in a range between -0.4 and 0.6×10^{-5} s^{-1}.

Table 1 lists the fraction of fronts with frontal-wave cyclogenesis as a function of their along-frontal stretching. For positive values, the fractions are highest in the range between 0 and

0.6×10^{-5} s^{-1} (bold). Negative stretching rates seem not to have a damping effect. However for increasing stretching rates above 0.6×10^{-5} s^{-1} the fraction of frontal waves with cyclogenesis starts to decrease. This is particularly pronounced for stretching rates greater than $1.2-1.4 \times 10^{-5}$ s^{-1}. Hence our data support the hypothesis that frontal-wave growth becomes unlikely at strain rates above $0.6-0.8 \times 10^{-5}$ s^{-1}.

However for along-frontal stretching rates of $2.0-2.5 \times 10^{-5}$ s^{-1} we still identify two cases, and one further outlier at 3.2×10^{-5} s^{-1} (not listed). It accounts for 0.35% of all fronts with stretching rates of a similar order. Given the limited number of cases in this very strong stretching regime, it is not clear whether the method used to calculate the along-frontal stretching is flawed in very strong situations (see the estimated error measure below), or if the assumptions made in the model of Bishop and Thorpe (1994a) do not apply any more, e.g. barotropic edge wave growths in a saturated environment. Therefore we cannot fully confirm with high confidence the hypothesis that all frontal-wave growth is suppressed for strain rates above 2.5×10^{-5} s^{-1}, but the vast majority are. The lack of statistical significance due to the limited number of cases in this strong stretching regime leaves room for future case-studies. Apart from this outlier, frontal-wave growth is inhibited for rates greater than 2.5×10^{-5} s^{-1}.

As outlined previously, Bishop (1996b) outlined an inversion method to identify the flow which is attributable to the vorticity and divergence outside a frontal box and the part inside a frontal box. He argues that the part of the flow outside the frontal box is representative of the along-frontal strain rates identified in analytical models. In this study the flow is decomposed into its divergence-free and irrotational component and the stretching is calculated along the gradient of the fronts based on the divergence-free component. The fronts are defined by contours of equivalent potential temperature. Dritschel *et al.* (1991) suggest that the ambient stretching be defined along contours of vorticity. The latter two methods probably show more sensitive results in the computation of the along-frontal strain compared to the inversion method suggested by Bishop (1996b). There is also some degree
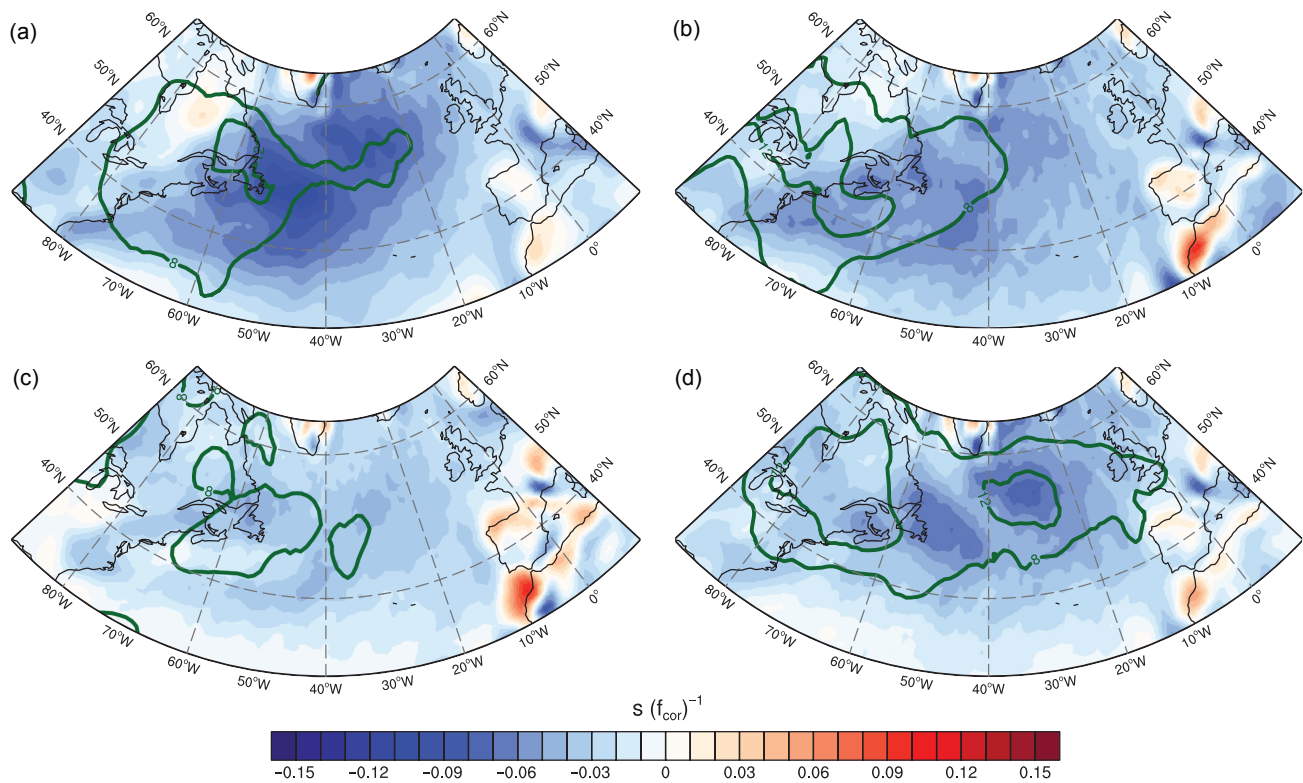
Figure 7. Seasonal climatologies of the dimensionless stretching rates of the ambient wind along equivalent potential temperature gradients at 850 hPa (see text for details) normalized by the Coriolis parameter. This parameter indicates preferred regions of frontal-wave growth for (a) DJF, (b) MAM, (c) JJA and (d) SON. Green contours indicate the fraction of frontal-wave cyclogenesis relative to all cyclogenesis (8 and 12%).

of arbitrariness in defining the along-frontal direction. However, to estimate the error associated with the chosen method in this study, the along-frontal strain rate is recalculated, but this time parallel to contours of vorticity at the identified trailing fronts. From the differences over three years, the absolute value of the mean error is estimated to be $0.05 \times 10^{-5}\,\mathrm{s}^{-1}$ for all frontal-wave cyclogenesis events and to be $0.2 \times 10^{-5}\,\mathrm{s}^{-1}$ for all trailing fronts without cyclogenesis. Hence the estimated range of strain rate above which frontal-wave growth becomes unlikely $(0.6 - 0.8 \times 10^{-5}\,\mathrm{s}^{-1})$ is associated with a relatively minor error.

A second hypothesis drawn from the findings of Bishop and Thorpe (1994b) is that '*There is always a strain rate that can completely suppress wave steepening. This is true even when the front has a structure that, in the absence of strain, would support infinite normal-mode growth rates*' (Bishop and Thorpe, 1994b, p. 881). The growth rate of a frontal wave is damped by a term in the growth equation which is proportionally to $2\alpha/f$, where α denotes the along-frontal stretching component of the ambient wind $(\partial v_a / \partial y_f)$ and f is the Coriolis parameter. Accordingly the fraction of frontal waves with cyclogenesis is limited by the climatological value of the normalized stretching rate $((\partial v_a / \partial y_f) f^{-1})$. If it is large, frontal-wave growth is unlikely to occur. To test this hypothesis, the along-frontal stretching is calculated for all fronts, but since the number of fronts was found to be insufficient to produce a proper climatology (note that the detected fronts are thin lines where the thermal front parameter is 0), we decided to present a climatology of the stretching rate parallel to $\nabla\theta_e$ on which the used front detection is based.

The normalized stretching rate is presented in Figure 7 and is compared to Figure 2, which shows the fraction of frontal-wave cyclogenesis to all cyclogenesis events. The findings of Bishop and Thorpe (1994b) suggest that the fraction of frontal-wave cyclogenesis[†] is higher in regions where the damping of frontal

waves is weak. In most regions of the NA, the normalized stretching rate parallel to the gradient of θ_e at 850 hPa is climatologically below 0. During DJF two regions with strongly negative values are apparent in the NA: east of Nova Scotia and southeast of Greenland. In both regions the fraction of frontal-wave cyclogenesis is enhanced compared to the rest of the NA. From Figure 2(a) we find east of Nova Scotia a relative portion of 12–14% and to the southeast of Greenland (22 °W, 53 °N) 10–12%. In the latter regions the two patterns are not in the exact same location, but if we assume that frontal-wave growth starts where the normalized stretching rate is low, the first closed contour is most likely detected downstream. Over land, the highest fraction of frontal-wave cyclogenesis in Figure 2(a) is identified over Newfoundland and Québec and bears no similarity to the normalized stretching climatology.

For MAM and JJA (Figure 4(b,c)) weakest stretching rates are identified in the western NA. The low rates in the western NA are in accordance with the fraction shown in Figure 2(b,c), however the linkage between the two fields is less clear than in DJF.

During SON (Figure 4(d)) the normalized stretching rates reveal two maxima, with lowest rates east of Nova Scotia and southeast of Greenland (similar but weaker than in DJF). Two maxima are also apparent in the fraction of frontal-wave cyclogenesis in Figure 2(c). The normalized frequency pattern is shifted slightly into the upstream direction (assuming westerly flow at Nova Scotia and northwesterly flow at Greenland). Higher fractions of frontal-wave cyclogenesis over land are not reflected in reduced stretching rates in Figure 4(d). However the result for DJF and SON in the central NA support the analytical findings drawn from the layered barotropic model of Bishop and Thorpe (1994b), i.e. frontal-wave development is limited by a factor proportional to the along-frontal stretching and normalized by the Coriolis parameter, while over land the fraction of frontal-wave cyclogenesis shows no clear relationship to the stretching climatology.

On average highest strain rates are associated with cases near land masses which, due to enhanced friction over land, likely introduce greater uncertainty in the calculation of the frontal orientations. This suggests that the highest correspondence

---

[†]It would also be appropriate to compare it to the ratio of trailing fronts with frontal waves on them to all trailing fronts, but the limited number of thin frontal lines detected in this study produces a very noisy climatology.

between stretching rates and frontal-wave cyclogenesis can be expected over the ocean.

7. Conclusions

Frontal instability is an important mechanism driving the initial formation and early growth of midlatitude cyclones. Cyclones emerging from frontal waves are typically smaller in size and are known to deepen rapidly (Parker, 1998). In this study we characterised cyclogenesis emerging on fronts in the North Atlantic sector from a climatological perspective. In particular the ambient conditions and the vertical structure of frontal-wave cyclogenesis are studied by means of composited analyses of selected fields. The findings are also compared to the assumptions made by earlier studies in idealised settings of frontal-wave growth. The characterization can act as a guide for the design of future idealised studies.

7.1. Climatology

Firstly frontal-wave cyclogenesis is localized by a combination of two automated identification schemes, one for fronts (Hewson, 1998; Jenkner et al., 2010; Schemm et al., 2014) and a second one for cyclones (Wernli and Schwierz, 2006). The latter includes a tracking scheme which allows identification of cyclogenesis defined as the occurrence of a first closed isobar in the sea-level pressure field. If cyclogenesis is identified on a front, it is regarded as a frontal-wave cyclogenesis if the front is trailing a parent cyclone. Any cyclone can act as parent cyclone except during its own genesis. The procedure therewith identifies synoptic situations which closely resemble scenarios discussed in previous studies on frontal-wave cyclogenesis. The presented seasonal climatologies revealed the following conclusions.

During the winter season (DJF), frontal-wave cyclogenesis is most frequent in the Gulf Stream region and over Newfoundland. The maximum fraction of frontal-wave cyclogenesis to total cyclogenesis in the Gulf Stream region is around 12–14%. In the central NA around 10% of all cyclogenesis events are classified as frontal-wave cyclogenesis. During MAM the differences to DJF are small, with the highest fraction of frontal-wave cyclogenesis becoming more confined to the Gulf Stream region and extending over land towards the Great Lakes. During the summer season (JJA), frontal-wave cyclogenesis is reduced over the NA; around 8–10% of all cyclone formations emerge from frontal waves in the central NA and over the Gulf Stream. During SON the fraction of frontal-wave cyclogenesis shows two maxima. Frontal-wave cyclogenesis accounts for 14–16% of all cyclone formations in the central NA (38°W, 54°N) and a similar high fraction is identified in a broader region which encompasses the Great Lakes, the Hudson Bay and Nova Scotia. Frontal-wave cyclogenesis in the former region is addressed for example in the case-studies by Renfrew et al. (1997) and Appenzeller and Davies (1996)

7.2. Horizontal structure

Frontal-wave cyclogenesis in the eastern (30–0°W, 35–55°N) and western (90–45°W, 25–50°N) NA are analysed independently. Horizontal composites centred at the location of frontal-wave cyclogenesis are used to characterise the ambient environmental conditions during frontal-wave cyclogenesis and the findings are compared to the assumptions made in previous idealised analyses of frontal waves. We anticipate the findings to act as a blueprint for the design of future frontal-wave studies, e.g. idealised numerical model experiments.

Frontal-wave cyclogenesis in the eastern and western NA have comparable low-level PV values (∼1 pvu). The mean over the samples appears to be slightly higher in the eastern NA (0.1 pvu), but the sample variability ($\sigma \sim 0.5$ pvu) suggests that frontal waves do not differ systematically between the two basins. After

a normalisation of the low-level PV anomalies by the standard deviation of the local PV climatology, stronger low-level PV anomalies are revealed in the eastern NA, i.e. PV anomalies stronger than twice the standard deviation of the seasonal PV climatological occur approximately in every second frontal-wave cyclogenesis in the eastern NA (50–60%), but only in every third in the western NA (30–40%).

With regard to deformation and vertical motion in the lower troposphere, we find in the eastern NA frontal-wave cyclogenesis is associated with stronger deformation rates ($\sim 10 \times 10^{-5}$ s^{-1}) compared to the western NA ($\sim 7 \times 10^{-5}$ s^{-1}). While the along-frontal horizontal wind is on average higher in the eastern NA, which is also suggested by stronger horizontal PV gradients, vertical motion in the lower troposphere is of similar magnitude in the two basins ($\sim$20 hPa h^{-1}). The enhanced deformation in the eastern NA seems to weaken the amplification of the wave.

The low-level averaged dry and moist static stability (900 to 850 hPa) revealed the ambient atmosphere as typically potentially unstable. Due to adiabatic cooling during the slantwise ascent along the front in combination with cooling (or weak heating) and moisture uptake from the ocean surface, air masses are typically saturated during cyclogenesis (average relative humidity value are around 90–95% in both basins). At the cyclogenesis location the atmosphere is close to neutral moist static stability and the ambient atmosphere is saturated in a narrow zone along the front below $\sim$ 700 hPa. These findings are consistent with the assumptions used in the analytical model of Thorpe and Emanuel (1985), Bishop and Thorpe (1994a) and Emanuel et al. (1987).

Precipitation rates are in a comparable range in the two basins. This is noteworthy since atmospheric moisture contents over the Gulf stream are climatological higher. Turning to the surface flux anomalies in the eastern NA, maximum anomalies of sensible and latent heat flux are out of phase in their locations on the warmer side of the front. Accordingly warm air advected to the north along the cold front is first cooled (or moderately heated) by the ocean surface while moisture uptake remains positive. Thereafter saturation occurs. As a result, the minimum latent heat flux anomaly is situated to the northeast of the minimum in the sensible heat flux.

7.3. Vertical structure

Consideration is also given to the vertical structure of frontal-wave cyclogenesis. To do so, composites of vertical cross-section in the along-front direction are analysed. We find frontal-wave cyclogenesis in the eastern NA associated with stronger PV anomalies in the upper troposphere than in the western NA. Furthermore, the lower- and upper-tropospheric PV anomalies penetrate deeper into the mid-troposphere in the eastern NA. Since frontal-wave cyclogenesis in the eastern NA is associated with stronger deformation strain, the enhanced upper- and lower-level PV anomalies are most likely required for frontal waves in the eastern NA to overcome the suppression by enhanced deformation strain (Fehlmann and Davies, 1999). Moreover it is noteworthy that frontal-wave cyclogenesis in the eastern NA reveals an advanced vertical alignment of upper- and lower-level PV anomalies, i.e. the vertical PV structure is more upright than cases in the western NA. This alignment suggests a more rapid deepening than in frontal-wave cyclogenesis in the western NA, due to an intensified phase-locking and mutual interaction between the two edge waves. A normalisation of the PV anomalies by the standard deviation of the seasonal PV climatology reveals PV anomalies at the tropopause level in the order of ∼1 std in the western NA and ∼1.5 std in the eastern NA. PV anomalies greater than two times the standard deviation of the seasonal PV climatology occur twice as often in the lower than in the upper troposphere in both basins.

Vertical motion is higher in the mid and upper troposphere in the western NA despite the stronger PV anomalies in the eastern

NA at upper and lower levels. We identify enhanced ice-water content in the mid and upper troposphere during frontal-wave cyclogenesis in the western NA, therefore latent heat release likely enhances vertical motion in the western NA.

7.4. Along-frontal stretching

Finally the multi-decadal analysis of the along-frontal stretching of the ambient wind, which is obtained from the divergence-free component of the two-dimensional wind field at 850 hPa, revealed *a Gaussian-shaped distribution of along-frontal stretching rates centred at $0.4 \times 10^{-5} s^{-1}$ for all trailing fronts above the ocean. If only frontal-wave cyclogenesis is considered, the distribution is more confined around $0.2 \times 10^{-5} s^{-1}$ and decreases more strongly than the full distribution at stretching rates above $0.6 - 0.8 \times 10^{-5} s^{-1}$.*

This is also reflected in the fraction of fronts with frontal-wave cyclogenesis as a function of along-frontal stretching. While for strain rates in a range from -0.2 to $0.6 \times 10^{-5} s^{-1}$ around $0.3 - 0.4\%$ of all trailing fronts form a cyclone; the fraction reduces systematically with increasing strain rates. Above $1.0 \times 10^{-5} s^{-1}$, the fraction is reduced by around a factor of 2 to $\sim 0.2\%$ of all trailing fronts with a similar strain rate and above $1.8 \times 10^{-5} s^{-1}$ to a fraction of $\sim 0.1\%$. For very strong stretching rates between 2.0 and $2.5 \times 10^{-5} s^{-1}$, two cases were identified. Only one single frontal-wave cyclogenesis was identified with strain rates greater than $3.0 \times 10^{-5} s^{-1}$.

Accordingly the presented analysis supports the hypothesis of Bishop and Thorpe (1994b), who suggested frontal-wave growth due to barotropic edge waves to be very unlikely for strain rates greater than $0.6 \times 10^{-5} s^{-1}$. However, according to their findings all frontal-wave growth is suppressed for along-frontal stretching rates greater than $2.5 \times 10^{-5} s^{-1}$, which due to the single outlier cannot be fully supported by our study. We note that, due to the limited number of cases identified in extremely strong stretching regimes $> 2.0 \times 10^{-5} s^{-1}$, the lack of statistical significance does not allow a final conclusion on the existence of this upper limit. Note that the temporal evolution and variation of along-frontal stretching might be important to frontal-wave cyclogenesis and future work may address this question utilizing frontal tracking methods, with a particular focus on cases with strong strain rates.

Finally we explored the geographical distribution of along-frontal stretching rates normalized by the Coriolis parameter. This coefficient is the limiting factor in the equation of frontal-wave growth in the idealised model of Bishop and Thorpe (1994b). To this end we compared the seasonal climatology, compiled from the along-frontal stretching along the gradients of θ_e at 850 hPa, with the frontal-wave cyclogenesis fraction. For DJF and SON over the ocean, we identified regions where the normalised along-frontal stretching is climatologically low and at the same time are in close vicinity to regions where the fraction of cyclogenesis forming on frontal waves is high. The differences in the location is most likely attributable to the detection of cyclogenesis, i.e. the formation of the first closed isobar, which occurs slightly after the break-up of the frontal-wave. No agreement is found for the frontal-wave fraction over land. Future work may address this issue using identification strategies based on vorticity criteria (Hewson, 2009).

7.5. Outlook

The presence of a pronounced upper-tropospheric PV anomaly suggests that the identified frontal-wave cyclogenesis in this study resides in the transformation phase during which the system translates from a barotropic into a baroclinic type of wave. We therefore argue that a detailed climatological investigation of the temporal evolution of an earlier period (± 12 h around the cyclogenesis) appears to suggest a promising follow-up to this study. For such a study, a vorticity-based cyclone detection approach appears to be useful as it detects cyclones earlier in their life cycle (Hewson, 2009).

Future work may also address the frontal-wave cyclogenesis under extreme strain rates ($> 2.5 \times 10^{-5} s^{-1}$) for which we identified one example. So far it is not clear whether the method used to compute the along-frontal stretching is flawed (although a manual analysis did not reveal an unusual synoptic situation) or the assumptions made in the barotropic model of Bishop and Thorpe (1994b) are violated.

Acknowledgements

Appendix A

Alignment of fronts in a south–north direction

For the computation of the horizontal composites, all trailing fronts are rotated so that they align in the south–north direction. The rotation is performed so that the distance sum between each frontal grid point and the y–axis is minimized. Here we briefly discuss the quality of the rotation. Figure A1 shows the horizontal composite of all trailing fronts after the rotation, i.e. every grid-point with a detected front is flagged by 1, all others by 0 and the mean over the sample is computed. From Figure A1 it becomes clear that the rotation performs well close to cyclogenesis in the centre of the domain. Only to the far north and south do the fronts tend to deviate from the y-axis and do not align properly along the south–north axis. This is simply due to the fact that fronts are not straight lines but are rather wavy. Nevertheless the result shows that, in at least a $\sim 5°$ radius around the frontal-wave cyclogenesis, the majority of frontal waves align well with the south–north axis.

Appendix B

Composites of relative humidity

Horizontal and vertical composites similar to Figures 3 and 5 are presented in Figure B1. The results are discussed in the main body of this study.
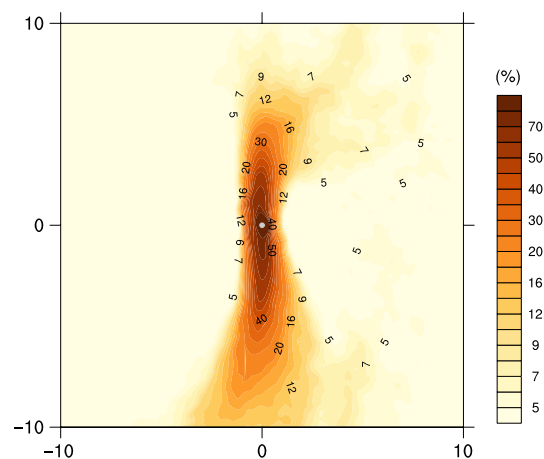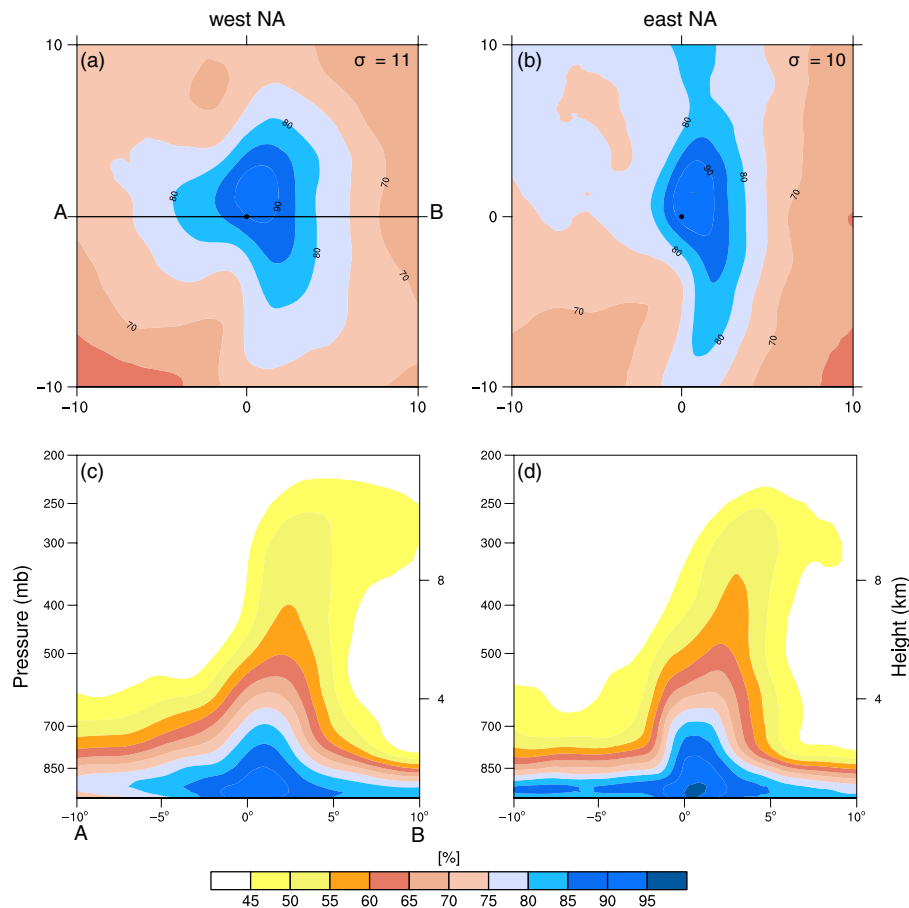

Figure A1. Horizontal composite (%) of rotated fronts.

Figure B1. (a,b) Horizontal and (c,d) vertical composites similar to Figures 3 and 5, but for relative humidity. Vertical cross-sections are across the front from A to B.

References

Appenzeller C, Davies HC. 1996. PV morphology of a frontal-wave development. *Meteorol. Atmos. Phys.* **58**: 21–40.

Ayrault F, Lalaurette F, Joly A, Loo C. 1995. North Atlantic ultra-high-frequency variability. *Tellus* **47A**: 671–696.

Baehr C, Pouponneau B, Ayrault F, Joly A. 1999. Dynamical characterization of the FASTEX cyclogenesis cases. *Q. J. R. Meteorol. Soc.* **125**: 3469–3494.

Bishop CH. 1996a. Domain-independent attribution. Part I: Reconstructing the wind from estimates of vorticity and divergence using free space Green's function. *J. Atmos. Sci.* **53**: 241–252.

Bishop CH. 1996b. Domain-independent attribution. Part II: Its value in the verification of dynamical theories of frontal waves and frontogenesis. *J. Atmos. Sci.* **53**: 253–262.

Bishop CH, Thorpe AJ. 1994a. Frontal wave stability during moist deformation frontogenesis. Part I: Linear wave dynamics. *J. Atmos. Sci.* **51**: 852–873.

Bishop CH, Thorpe AJ. 1994b. Frontal wave stability during moist deformation frontogenesis. Part II: The suppression of nonlinear wave development. *J. Atmos. Sci.* **51**: 874–888.

Bjerknes J, Solberg H. 1922. Life cycle of cyclones and the polar front theory of atmospheric circulation. *Geofys. Publ.* **3**: 3–18.

Čampa J, Wernli H. 2012. A PV perspective on the vertical structure of mature midlatitude cyclones in the Northern Hemisphere. *J. Atmos. Sci.* **69**: 725–740.

Chaboureau JP, Thorpe AJ. 1999. Frontogenesis and the development of secondary wave cyclones in FASTEX. *Q. J. R. Meteorol. Soc.* **125**: 925–940.

Dacre HF, Gray SL. 2006. Life-cycle simulations of shallow frontal waves and the impact of deformation strain. *Q. J. R. Meteorol. Soc.* **132**: 2171–2190.

Dacre HF, Gray SL. 2009. The spatial distribution and evolution characteristics of north atlantic cyclones. *Mon. Weather Rev.* **137**: 99–115.

Davies HC, Rossa AM. 1998. PV frontogenesis and upper-tropospheric fronts. *Mon. Weather Rev.* **126**: 1528–1539.

Davis CA, Emanuel KA. 1991. Potential vorticity diagnostics of cyclogenesis. *Mon. Weather Rev.* **119**: 1929–1953.

Dee DP, Uppala SM, Simmons AJ, Berrisford P, Poli P, Kobayashi S, Andrae U, Balmaseda MA, Balsamo G, Bauer P, Bechtold P, Beljaars ACM, van de Berg L, Bidlot J, Bormann N, Delsol C, Dragani R, Fuentes M, Geer AJ, Haimberger L, Healy SB, Hersbach H, Hólm EV, Isaksen L, Kållberg P, Köhler M, Matricardi M, McNally AP, Monge-Sanz BM, Morcrette J-J, Park BK, Peubey C, de Rosnay P, Tavolato C, Thépaut J-N, Vitart F. 2011. The ERA-Interim reanalysis: Configuration and performance of the data assimilation system. *Q. J. R. Meteorol. Soc.* **137**: 553–597, doi: 10.1002/qj.828.

Dritschel DG, Haynes PH, Juckes MN, Shepherd TG. 1991. The stability of a two-dimensional vorticity filament under uniform strain. *J. Fluid Mech.* **230**: 647–665.

Eliassen A, Kleinschmied E. 1957. Dynamic meteorology. In *Handbuch der Physik*, Flügge S. (ed.): 1–154. Springer-Verlag: Berlin.

Emanuel KA, Fantini M, Thorpe AJ. 1987. Baroclinic instability in an environment of small stability to slantwise moist convection. Part I: Two-dimensional models. *J. Atmos. Sci.* **44**: 1559–1573.

Fehlmann R, Davies HC. 1999. Role of salient potential-vorticity elements in an event of frontal-wave cyclogenesis. *Q. J. R. Meteorol. Soc.* **125**: 1801–1824.

Hewson TD. 1998. Objective fronts. *Meteorol. Appl.* **5**: 37–65.

Hewson TD. 2009. Diminutive frontal waves –a link between fronts and cyclones. *J. Atmos. Sci.* **66**: 116–132.

Hoskins BJ, Berrisford P. 1988. A potential vorticity perspective of the storm of 15–16 October 1987. *Weather* **43**: 122–129.

Hoskins BJ, McIntyre ME, Robertson WA. 1985. On the use and significance of isentropic potential vorticity maps. *Q. J. R. Meteorol. Soc.* **111**: 11–37.

Jenkner JM, Sprenger M, Schwierz C, Dierer S, Leuenberger D. 2010. Detection and climatology of fronts in a high-resolution model reanalysis over the Alps. *Met. Appl.* **17**: 1–8.

Joly A, Thorpe AJ. 1990. Frontal instability generated by tropospheric potential vorticity anomalies. *Q. J. R. Meteorol. Soc.* **116**: 525–560.

Lynch P. 1988. Deducing the wind from vorticity and divergence. *Mon. Weather Rev.* **116**: 86–93.

Malardel S, Joly A, Courbet F, Courtier P. 1993. Nonlinear evolution of ordinary frontal waves induced by low-level potential vorticity anomalies. *Q. J. R. Meteorol. Soc.* **119**: 681–713.

NCL. 2014. 'The NCAR Command Language version 6.2.1 [Software]'. UCAR/NCAR/CISL/VETS: Boulder, CO, doi: 10.5065/D6WD3XH5.

Parker DJ. 1998. Secondary frontal waves in the North Atlantic region: A dynamical perspective of current ideas. *Q. J. R. Meteorol. Soc.* **124**: 829–856.

Reed RJ, Grell GA, Kuo YH. 1993. The ERICA IOP5 storm. Part II: Sensitivity tests and further diagnosis based on model output. *Mon. Weather Rev.* **121**: 1595–1612.

Renfrew AI, Thorpe AJ, Bishop CH. 1997. The role of the environmental flow in the development of secondary frontal cyclones. *Q. J. R. Meteorol. Soc.* **123**: 1653–1675.

Rivals H, Cammas JP, Renfrew IA. 1998. Secondary cyclogenesis: The initiation phase of a frontal wave observed over the eastern Atlantic. *Q. J. R. Meteorol. Soc.* **124**: 243–267.

ⓒ 2015 The Authors. *Quarterly Journal of the Royal Meteorological Society* published by John Wiley & Sons Ltd on behalf of the Royal Meteorological Society.

Q. J. R. Meteorol. Soc. **141**: 2989–3005 (2015)

Schär C, Davies HC. 1990. An instability of mature cold fronts. *J. Atmos. Sci.* **47**: 929–950.

Schemm S, Wernli H. 2014. The linkage between the warm and the cold conveyor belts in an idealized extratropical cyclone. *J. Atmos. Sci.* **71**: 1443–1459.

Schemm S, Rudeva I, Simmonds I. 2014. Extratropical fronts in the lower troposphere –global perspectives obtained from two automated methods. *Q. J. R. Meteorol. Soc.* doi:10.1002/qj.2471.

Simmonds I, Keay K, Bye JAT. 2012. Identification and climatology of Southern Hemisphere mobile fronts in a modern reanalysis. *J. Clim.* **25**: 1945–1962.

Steppeler J, Doms G, Schäettler U, Bitzer HW, Gassmann A, Damrath U, Gregoric G. 2003. Meso-gamma-scale forecasts using the non-hydrostatic model LM. *Meteorol. Atmos. Phys.* **82**: 75–96.

Stoelinga MT. 1996. A potential vorticity-based study on the role of diabatic heating and friction in a numerically simulated baroclinic cyclone. *Mon. Weather Rev.* **124**: 849–874.

Thorpe AJ, Emanuel KA. 1985. Frontogenesis in the presence of small stability to slantwise convection. *J. Atmos. Sci.* **42**: 1809–1824.

Wernli H, Davies HC. 1997. A Lagrangian-based analysis of extratropical cyclones. II: A detailed case-study. *Q. J. R. Meteorol. Soc.* **123**: 1677–1706.

Wernli H, Schwierz C. 2006. Surface cyclones in the ERA-40 dataset (1958-2001). Part I: Novel identification method and global climatology. *J. Atmos. Sci.* **63**: 2486–2507.

Wernli H, Dirren S, Liniger MA, Zillig M. 2002. Dynamical aspects of the life cycle of the winter storm *Lothar* (24–26 December 1999). *Q. J. R. Meteorol. Soc.* **128**: 405–429.
[Correction added on 27 July 2015, after first online publication: The year of the reference "Wernli H, Dirren S, et al.", was previously wrong and this has been amended to 2002.]

Zhang DL, Cheng WY, Gyakum JR. 2002. The impact of various potential-vorticity anomalies on multiple frontal cyclogenesis events. *Q. J. R. Meteorol. Soc.* **128**: 1847–1877.